NASA/TP-20260000227

Haystack Ultrawideband Satellite Imaging Radar Measurements of the Orbital Debris Environment: 2022

Orbital Debris Program Office

James Murray
Nexus-Mb Solutions – Jacobs JETS II Contract

Jessica Arnold Headstream
NASA Johnson Space Center

Alyssa Manis
NASA Johnson Space Center

January 2026

NASA STI Program Report Series

The NASA STI Program collects, organizes, provides for archiving, and disseminates NASA's STI. The NASA STI program provides access to the NTRS Registered and its public interface, the NASA Technical Reports Server, thus providing one of the largest collections of aeronautical and space science STI in the world. Results are published in both non-NASA channels and by NASA in the NASA STI Report Series, which includes the following report types:

- TECHNICAL PUBLICATION. Reports of completed research or a major significant phase of research that present the results of NASA Programs and include extensive data or theoretical analysis. Includes compilations of significant scientific and technical data and information deemed to be of continuing reference value. NASA counter-part of peer-reviewed formal professional papers but has less stringent limitations on manuscript length and extent of graphic presentations.

- TECHNICAL MEMORANDUM. Scientific and technical findings that are preliminary or of specialized interest, e.g., quick release reports, working papers, and bibliographies that contain minimal annotation. Does not contain extensive analysis.

- CONTRACTOR REPORT. Scientific and technical findings by NASA-sponsored contractors and grantees.

- CONFERENCE PUBLICATION. Collected papers from scientific and technical conferences, symposia, seminars, or other meetings sponsored or co-sponsored by NASA.

- SPECIAL PUBLICATION. Scientific, technical, or historical information from NASA programs, projects, and missions, often concerned with subjects having substantial public interest.

- TECHNICAL TRANSLATION. English-language translations of foreign scientific and technical material pertinent to NASA's mission.

Specialized services also include organizing and publishing research results, distributing specialized research announcements and feeds, providing information desk and personal search support, and enabling data exchange services.

For more information about the NASA STI program, see the following:

- Access the NASA STI program home page at http://www.sti.nasa.gov

- Help desk contact information:

https://www.sti.nasa.gov/sti-contact-form/
and select the "General" help request type.

NASA/TP-20260000227

Haystack Ultrawideband Satellite Imaging Radar Measurements of the Orbital Debris Environment: 2022

Orbital Debris Program Office

James Murray
Nexus-Mb Solutions – Jacobs JETS II Contract

Jessica Arnold Headstream
NASA Johnson Space Center

Alyssa Manis
NASA Johnson Space Center

National Aeronautics and
Space Administration

Johnson Space Center
Houston, Texas 77058

January 2026

ACKNOWLEDGEMENTS

The authors would like to thank Quanette Juarez for her contributions to the data processing and data quality control efforts. Additionally, the authors would like to thank J.-C. Liou for a thorough review of the technical content of this report and Tim Kennedy for his contributions to analysis of the data. We would like to thank Debra Shoots and Ashley Johnson for their invaluable editing contributions.

This report is available in electronic form at
http://ntrs.nasa.gov/citations/20260000227

TABLE OF CONTENTS

SECTION **PAGE**

FIGURES

TABLES

TABLE **PAGE**

Acronyms

ΔRCS	Radar cross section calibration constants
AZ	Azimuth
CY	Calendar Year
CR	Continuous Record
CW	Continuous Wave
dB	Decibels
dBsm	Square meters measured in decibels
DRADIS	Debris Radar Automated Data Inspection System
EL	Elevation
FFT	Fast Fourier Transform
FY	Fiscal Year
GEO	Geosynchronous Orbit
HUSIR	Haystack Ultrawideband Satellite Imaging Radar
I	In-phase
JSC	Johnson Space Center
LEO	Low Earth Orbit
MIT/LL	Massachusetts Institute of Technology/Lincoln Laboratory
NaK	Sodium-Potassium
NASA	National Aeronautics and Space Administration
NWF	New Waveform
OD	Orbital Debris
ODPO	Orbital Debris Program Office
OP	Orthogonal Polarization
PP	Principal Polarization
Q	Quadrature, Quadrature-phase
RCS	Radar Cross Section (typically reported in dBsm)
RDI	Range Doppler Image
RFI	Radio Frequency Interference
RORSAT	Radar Ocean Reconnaissance SATellites
SEM	Size Estimation Model
SENS	Sensitivity
SNR	Signal-to-Noise Ratio
SSN	U.S. Space Surveillance Network
TLE	Two-line Element Set
TWT	Traveling Wave Tube

WFC	Waveform Code
XSNR	Excess SNR

(This page intentionally left blank)

1.0 Introduction

1.1 PURPOSE

This report summarizes radar measurement data of the orbital debris (OD) environment in low Earth orbit (LEO) from the Haystack Ultrawideband Satellite Imaging Radar (HUSIR) operated by the Massachusetts Institute of Technology's Lincoln Laboratory (MIT/LL) and the U.S. Department of Defense and provided to the National Aeronautics and Space Administration (NASA) Orbital Debris Program Office (ODPO).

1.2 SCOPE

The period covered by this report includes data collected during calendar year (CY) 2022. Additionally, data from CY2021 and CY2020 are included for year-to-year comparison purposes. Results presented in this report represent a broad overview of the current state of the OD environment in LEO as measured by HUSIR.

1.3 OVERVIEW

The NASA ODPO relies primarily on ground-based radar measurements to characterize the distribution of small debris in LEO (altitude < 2000 km) down to limiting sizes determined by the sensitivities of each radar. Since 1990, MIT/LL has collected radar measurements for the ODPO under agreements with NASA and the U.S. Department of Defense [1]. For over 30 years, the Haystack radar, renamed HUSIR after upgrades and a return to operations in 2014, has been the ODPO's primary source of OD radar data. As of U.S. Government Fiscal Year (FY) 2020, the ODPO receives nominally 500 hours of data from MIT/LL. For OD measurements, HUSIR operates in a stare mode designed to statistically sample objects in LEO smaller than those typically tracked and cataloged by the U.S. Space Command's Space Surveillance Network (SSN).

Historically, the ODPO has used HUSIR to sample the OD environment down to approximately 5.5 mm to an altitude of up to 1000 km and 2 to 3 cm throughout LEO. The data collected by HUSIR is used to characterize the OD environment in altitude, inclination, and size for a large fraction of LEO – limited by the latitude, pointing geometry, and sensitivity of the radar – including circular orbits in LEO and eccentric orbits traversing LEO.

This report includes an overview of HUSIR's radar systems, radar signal processing, radar measurements, and environment characterization. Some background information, originally presented in previous HUSIR radar reports, is repeated here for the benefit of the reader.

2.0 Radar System Overview

Located in Westford, Massachusetts, the HUSIR radar is of a Cassegrain configuration with a focus at the coordinates described in Table 2-1.

Table 2-1: HUSIR Location with Respect to the 1984 World Geodetic System (WGS 84) Earth Model

	Latitude	Longitude	Elevation
HUSIR	42.623287° N	288.511846° E	115.69 m

The HUSIR radar consists of a 36.6 meter-diameter parabolic reflector transmitting right-hand circularly polarized waveforms and receiving both right- and left-hand circularly polarized returns, representing the orthogonal polarization (OP) and principal polarization (PP) channels, respectively, of the radar. The waveform for OD measurements, referred to internally as waveform code 4 (WFC-4), consists of transmitting a pulsed continuous wave (CW) signal at X-band with a center frequency of 10.1 GHz. The operating parameters of WFC-4 are found in Table 2-2. Other waveforms of interest are WFC-1 and -11, which are used to calibrate the radar. Additional details are provided in section 3.0.

Table 2-2: Radar Debris Mode Nominal Operating Parameters

Operating Parameter	HUSIR
Peak Power (kW)	250
Transmitter Frequency (GHz)	10.1
Transmitter Wavelength (cm)	3.0
Antenna Diameter (m)	36.6
Antenna Half-power Beamwidth (deg)	0.058
Antenna Gain (dB)	67.23
System Temperature (K)	186
Total System Losses (dB)	3.9
Waveform Code (WFC)	4
Range Gates	16
Intermediate Frequency Bandwidth (kHz)	1250
Independent Range/Doppler Samples	15158
FFT Size	16384
Number of non-coherently integrated pulses used for detection	16
Pulse Width (msec)	1.6384
Receive Window (msec)	12.1264
Pulse Repetition Frequency (Hz)	60
Nominal Sensitivity (dB)	59.2
Average Power (kW)	24.6
Doppler Extent (km/s)	±7.5

The HUSIR radar also features a monopulse feed horn capable of estimating object position in the beam with a single pulse using amplitude-comparison monopulse techniques. While traditionally used to maintain tracked objects on boresight, now the ODPO uses monopulse to estimate an object's path through the beam while the radar remains stationary (beam-park mode).

The 16 range gates, referenced in Table 2-2, are used in the initial detections performed by MIT/LL with their real-time processor, discussed in section 3.0. Subsequent processing of the data by the ODPO uses a higher number of range gates to reduce the effects of range discretization.

In previous years, a 10 GHz debris waveform was used. To combat increasingly prevalent radio frequency interference (RFI) at 10 GHz, MIT/LL developed a new waveform (NWF) with a center frequency of 10.1 GHz in CY2020. To validate the performance of this NWF, data was taken at both 10 GHz and 10.1 GHz center frequencies in CY2020 and CY2021. The 10.1 GHz waveform was shown to produce data comparable to the 10 GHz waveform [2]. Following the analysis of 10.1 GHz data from CY2020 and CY2021, the ODPO directed MIT/LL to use the 10.1 GHz waveform exclusively after 01 October 2021. The NWF has proven highly effective; the 10.1 GHz data experienced no RFI contamination in CY2021 or CY2022. Therefore, the CY2022 data presented in this report consists only of data collected with the NWF. In comparison charts with the previous years' data the 10 GHz waveform data and 10.1 GHz NWF data have been combined.

2.1 RADAR PERFORMANCE

The nominal sensitivity of HUSIR is 59.2 decibels (dB), where sensitivity is defined as the single pulse signal-to-noise ratio (SNR) for an object with a radar cross section (RCS) of 1 square meter (0 dBsm) at 1000 km slant range. Of the operating parameters that significantly affect sensitivity, transmit power is the most variable, and understanding its history over the CY is useful. Figure 2-1 shows the transmitted power history of HUSIR during CY2022 at 10.1 GHz. Transmit powers less than 140 kW correspond to periods when HUSIR operated with 3 traveling wave tubes (TWT) rather than all four TWTs, and lower than nominal power may indicate burn-in periods for new tubes after replacement.

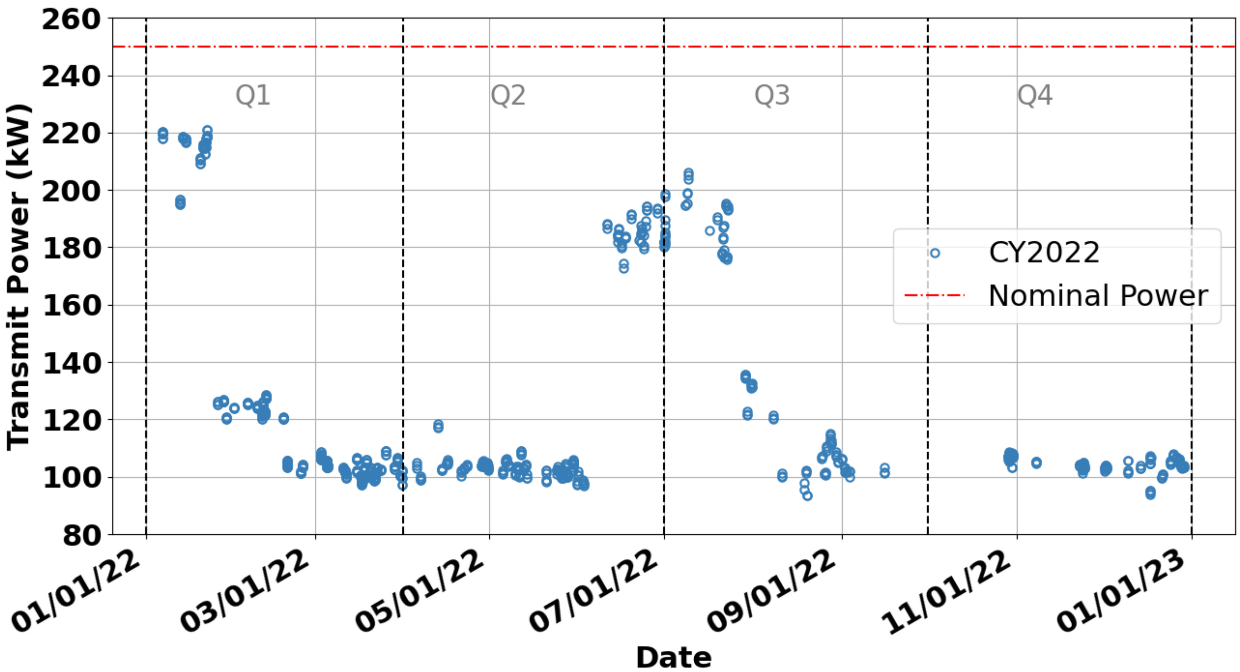

Figure 2-1: HUSIR CY2022 transmit power history. The red horizontal dash-dotted line represents the nominal HUSIR transmit power of 250 kW.

The altitude-dependent size of debris detectable by HUSIR is determined by sensitivity and staring geometry. There are three staring geometries employed by the ODPO; 75° elevation, due East (75E); 20° elevation, due South (20S); and 10° elevation, due South (10S). These geometries are discussed further in Section 3.0. Figure 2-2 shows the sensitivity curves of HUSIR CY2022 75E data at 10.1 GHz to 99%, 95%, and 90% completeness levels, which are overlaid on a scatter plot of orbit altitude versus Size Estimation Model (SEM) size for the dataset. These completeness curves are estimated from the data and represent the altitude-dependent size to which the data is estimated to be complete at each indicated level; a complete description of the methodology is presented in Appendix B of [3]. These curves represent the altitude-dependent size at which the prescribed percentage of objects passing through the beam are detected. From Figure 2-2, the HUSIR CY2022 75E data at 10.1 GHz is approximately 99% complete down to a size of 7.2 mm at 1000 km altitude. Table 2-3 shows the sensitivity at 1000 km for HUSIR CY2022 75E datasets to 99%, 95%, and 90% levels of completeness. The amount of south staring data was insufficient to accurately determine data completeness.

Table 2-3. Sensitivity at 1000 km for CY2022 75E Datasets to 99%, 95%, and 90% Levels of Completeness

Completeness	75E 10.1 GHz
99%	7.2 mm
95%	6.5 mm
90%	6.2 mm

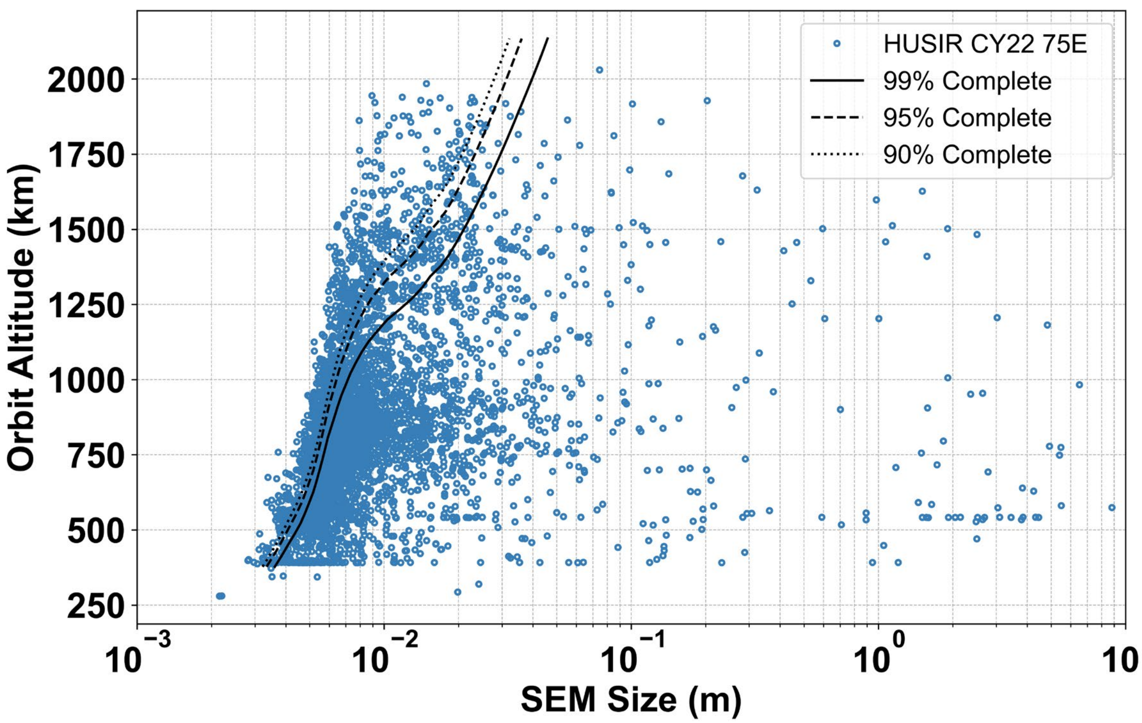

Figure 2-2: Orbit altitude versus SEM size for HUSIR CY2022 75 E data with 99%, 95%, and 90% completeness curves.

3.0 Radar Processing and Data Collection

For OD radar data collection, HUSIR operates in a "beam-park" mode where the radar antenna is pointed at a fixed elevation (EL) and azimuth (AZ), allowing portions of the debris environment to pass through the radar beam. This provides a fixed detection volume that simplifies calculations of the debris flux, or number of objects detected per unit area, per unit time. Since the radar does not change its pointing in beam-park mode and the radar beam has a 0.058° beamwidth, the observation time is short, and relatively few pulses are collected on each object. Although this limits the precise measurement of a detected object's orbital parameters, the pointing geometry can provide meaningful orbital information.

Typically, OD radar data is collected in one of three staring geometries: 75E, 20S, and 10S. By staring just off-zenith, the 75E staring geometry allows the radar to measure Doppler shifts that give meaningful orbital information for orbital inclinations between approximately 40° inclination and 140° inclination using a circular orbit approximation. The 75E staring geometry comprises approximately two-thirds of the total observation time spent collecting OD radar data from HUSIR each year. The remaining third of observation time is split approximately evenly between the 10S and 20S geometries. Although these geometries suffer from reduced sensitivity due to increased atmospheric attenuation and longer path length for a given altitude, they allow HUSIR to view lower orbital inclinations down to approximately 20 degrees.

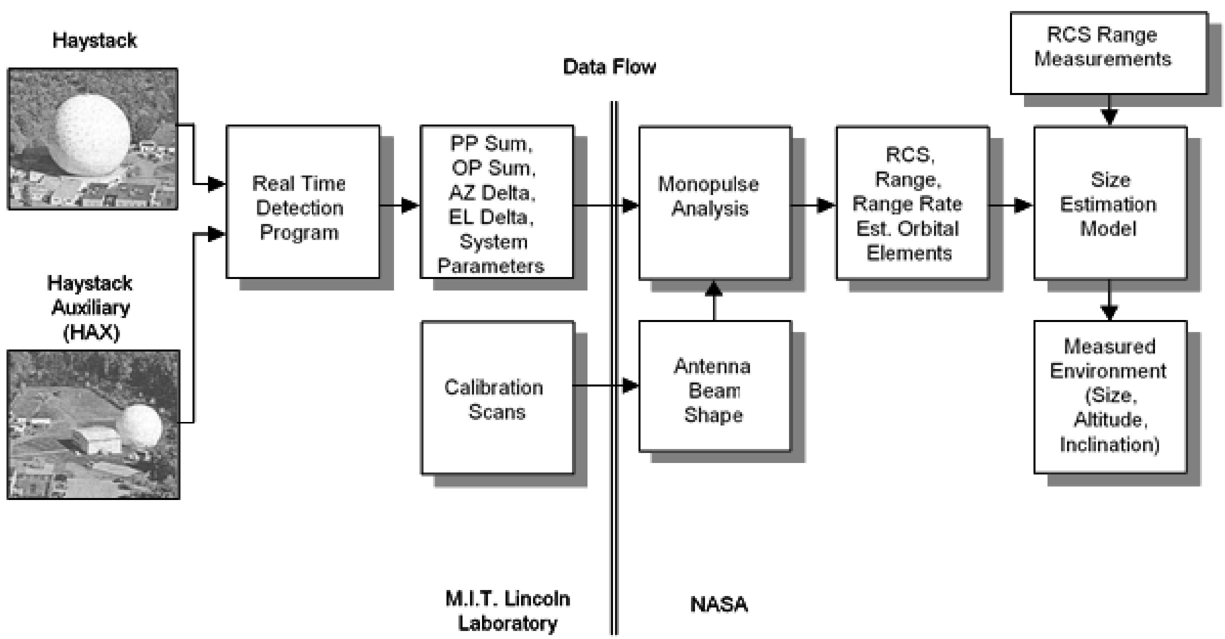

M.I.T. Lincoln Laboratory ***NASA Johnson Space Center***

Figure 3-1: An overview of the data collection and analysis. Images reprinted with permission of MIT/LL, Lexington, Massachusetts. As of CY2022 Q4, the real time detection program has been replaced with a continuous record system.

Figure 3-1 gives an overview of the data collection and analysis performed by MIT/LL and the ODPO. At the radar, MIT/LL employs a continuous record system that mimics the previous real-time target detection program. Details of this new recording system are discussed later in this section. Data is recorded to an excised continuous record file only when the integrated SNR exceeds a predetermined threshold in the PP channel. If the threshold remains exceeded, the buffer continues to record pulses. Additionally, several pulses from before and after the threshold was exceeded are recorded to minimize the loss of useful data and define the noise background.

MIT/LL performs regular calibration scans in the form of calibration sphere tracks (.S files) and spiral scans (.R files) in addition to the debris mode observations. These are nominally performed at the beginning and end of debris data collects using a WFC combination of WFC-11 for tracking and WFC-1 for calibration measurements, as illustrated in Figure 3-2. Additional details regarding the calibration sphere tracks and spiral scans are discussed in Sections 3.3 and 3.4.

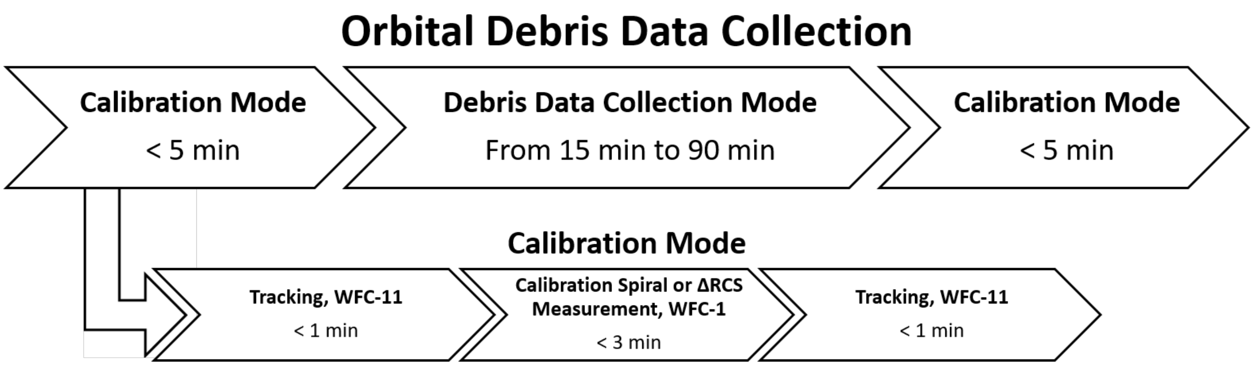

Figure 3-2: Orbital debris data collection and pre- and post-data collection timeline. MIT/LL conducts the object track using the narrow band WFC-11. They conduct the beam shape calibration spiral using the CW WFC-1. One or more calibration mode segments may be conducted before and after one or more data collection mode segments.

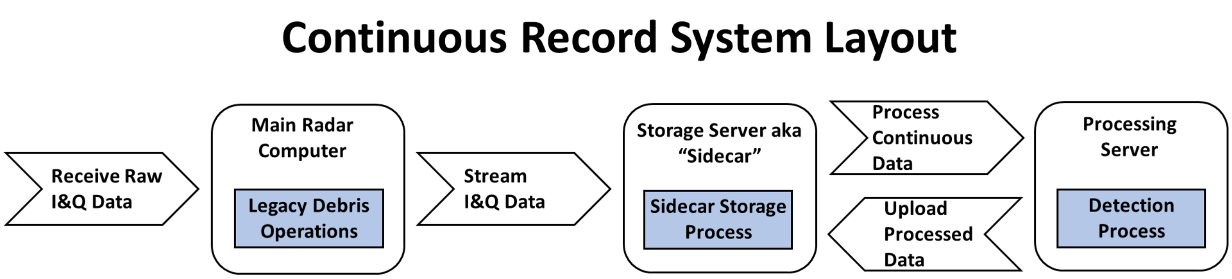

Figure 3-3: Layout of the continuous record system and summary of processes. From 2020 Q1 to 2022 Q3 the continuous record process ran simultaneously with the real-time legacy debris operations.

In CY2022, Q4 data collection moved away from the legacy real-time detection system to a continuous record (CR) system. During legacy debris operations, data was only recorded to a debris data file upon hit detections. In 2020 Q1, MIT/LL began testing a CR system that records all data to a storage server and excises detections to a debris data file during post-processing. The main advantage of the CR system is that it allows for post-processing not feasible with the real-time system, including implementing multiple detection algorithms and detection of transmitter dropout. It also allows the raw data to be revisited. A layout of the CR system is shown in Figure 3-3. The legacy and CR systems were used in parallel during 2020 Q1 – 2022 Q3 debris operations. The CR system has been demonstrated to produce data of the same quality as the legacy real-time system.

3.1 RADAR SIGNAL PROCESSING AT JOHNSON SPACE CENTER

The ODPO performs radar signal processing at the Johnson Space Center (JSC) using the in-house developed Debris Radar Automated Data Inspection System (DRADIS). DRADIS is a tested and validated software tool used to process data from FY2014 to present. All CY2022 data presented in this report was processed using DRADIS version 1.5.0.

To process data from MIT/LL using DRADIS, several signal processing parameters must be set. Table 3-1 lists these signal processing parameters, the stage of the processing each parameter is associated with, and the values used to detect and measure OD in the observations presented in this report.

Table 3-1: DRADIS Signal Processing Parameters

Processing Parameter	Value
Range Doppler Image	
FFT Size	Zero-padded to 16384 samples
Observation Length	2048 samples
Number of Range Gates	32
Weighting/Windowing	None/Rectangle
Detection	
Detector Type	Non-coherent Integration
Detection Channel	PP
Number of pulses integrated	16
Detection SNR Threshold	5.65 dB
Monopulse Threshold	11 dB
FFT Peak Interpolation	False
Measurement	
Measurement FFT Size	Zero-padded to 16384 samples
FFT Peak Interpolation	True
Monopulse Mode	Legacy
Matched Filter Least Squares Fit	False
Use Integrated Range	True
Validation	
Valid SNR Threshold	5.65 dB

In addition to DRADIS, several other post-processing techniques have been implemented to improve the quality and consistency of data from year to year. As a general overview, the steps involved to produce the final data set in this report are:

1) MIT/LL collects OD radar data, producing debris, spiral scan, and sphere track data files, which are recorded by MIT/LL and transferred to JSC. Additional details regarding OD radar data collection are summarized in Figure 3-1.

2) Debris data files are batch processed with DRADIS using spiral scan files as calibration inputs.

    a. Spiral scan calibrations can be overridden to use an average beam shape model when spiral scan sensitivity is insufficient to produce an accurate beam shape calibration.

3) Sphere track files are processed through DRADIS calibration routines to independently produce sensitivity (SENS) files that contain calibration constants (ΔRCS) for the debris files.

    a. These are compared to SENS files provided by MIT/LL to ensure consistency.

4) Individual detection files produced by DRADIS are compiled into annual detection lists and include all pointing geometries for the radar.

5) Manual RFI review is performed on all detections by inspecting pulse-by-pulse range versus range-rate plots.

    a. All detections determined to contain RFI are transferred to a separate “removed” list.

6) The annual detection list is split into separate detection lists for each pointing geometry.

    a. Subsequent processing is dependent on pointing-specific parameters.

7) A polarization filter for sodium-potassium (NaK) discrimination is defined based on polarization, altitude, and Doppler-derived inclination associated with NaK orbits.

8) Calibration quality is checked using the PP RCS clustering characteristics of the NaK debris population, which are nominally sphere-shaped electrical conductor particles. The PP RCS should be related to the peak in the resonance region for the monostatic RCS from a conducting sphere [4].

    a. When enough detections are available, data that appears to be biased in PP RCS away from the expected peak are removed from the detection list and placed on the removed list.

9) The raw detection rates of detection files with zero valid detections are compared to the raw detection rates of detection files containing valid detections to verify the no-detection measurement is valid. Zero valid detections can be a valid measurement, especially for low-elevation HUSIR observations. Due to their lower sensitivity, such observations

typically have low overall counts, despite the larger collection area, leading to low detection rates relative to the duration of the observation windows.

   a. Detection files with out-of-family raw detection rates are removed from the dataset, and the corresponding observations hours are placed on the removed list.
   b. Raw detection rate refers to the detection rate of the real-time processor that operates with a lower SNR threshold than is used by DRADIS.

10) Each detection is compared to the SSN satellite catalog to determine if any detection correlates with a cataloged object. The measured RCS of correlated detections are compared to the SSN RCS histories of the cataloged objects to identify sidelobe detections.
   a. Detections determined to be sidelobe detections are removed from the detection list and placed on the removed list.
11) A standard set of charts are generated for inspection by OD subject matter experts. These charts illustrate the behavior of the data set over relevant radar and detected object parameters including range, range-rate, RCS, NASA SEM-estimated size, SNR, Doppler inclination, and altitude.
12) Standard chart sets are compared with previous annual data sets and/or contemporaneous data sets from other sensors to ensure behavior is consistent and/or differences are understood.
13) Once all differences are understood, a final detection list is placed under configuration management to be used by teams modeling the OD environment.

Additional details about the individual steps outlined above are presented in the following sections.

3.2 DRADIS PROCESSING

A high-level overview of the operations performed by DRADIS during the processing of debris data files is shown in Figure 3-4. DRADIS employs a multi-pass approach consisting of a detection pass and two measurement passes. The detection pass generates a range Doppler image (RDI) from the in-phase (I) and quadrature-phase (Q) samples and applies an SNR threshold to determine whether an object is present using the user-specified processing parameters, as shown in Table 3-1. Initial estimates of the Doppler frequency, SNR, and approximate sample offset in the range gate containing the detection are made during the detection pass and used as inputs to the first measurement pass. The first measurement pass occurs at the individual detection level and provides measurements such as range, range-rate, monopulse voltage ratios, monopulse angle offsets, and PP and OP RCS on a pulse-by-pulse basis.

The second measurement pass occurs at the detection group level and uses information from all pulses within a detection group to estimate the object's path through the beam and make estimates of the target's orbital elements and target parameters. These include the object's range and range-rate; PP and OP SNR; Doppler-derived orbit inclination; beam path-corrected PP and

OP RCS; and the NASA SEM-generated size estimate. Detailed descriptions of the detection and measurement passes can be found in Section 3.2 of [5].

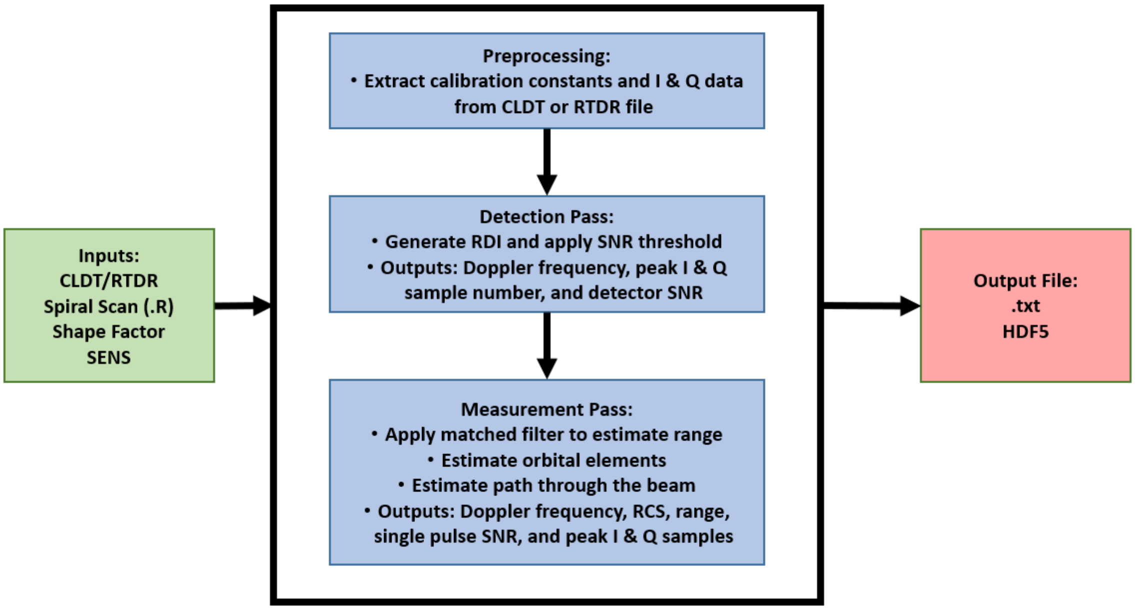

Figure 3-4: Overview of the radar data processing conducted by DRADIS.

3.3 SPHERE TRACK CALIBRATION

The operators at MIT/LL regularly perform end-to-end calibration of the radar system to minimize measurement errors. Several times a day the operators track and measure the RCS of known calibration spheres as they pass through the radar field of view. These include calibration spheres with SSN object numbers: 39490 (COSMOS 2493 (SKRL 756)), 900 (CALSPHERE 1), 902 (CALSPHERE 2), 1512 (TEMPSAT 1), 1520 (CALSPHERE 4A), 2826 (OPS 5712 (P/L 160)), and 5398 (RIGIDSPHERE 2 (LCS 4)). A correction factor, known as the ΔRCS, is calculated from the difference of the measured RCS and the known RCS of the given sphere (in decibels), as shown in the following equation:

$$\Delta RCS = RCS_{measured} - RCS_{theoretical}$$

This process is carried out before every OD radar data collection, and the ΔRCS is applied in post-processing to the collected data. Figure 3-5 shows a plot of the ΔRCS versus mean elevation for sphere track calibrations collected in CY2022, where mean elevation is the average elevation reported by the encoder during the observation.

Only the PP channel can be calibrated using the sphere track method due to the scattering properties of the calibration objects, which are metallic spheres. MIT/LL periodically calibrates the magnitude and phase error of the OP channel relative to the PP channel by injecting a calibration signal into both the PP and OP channels.

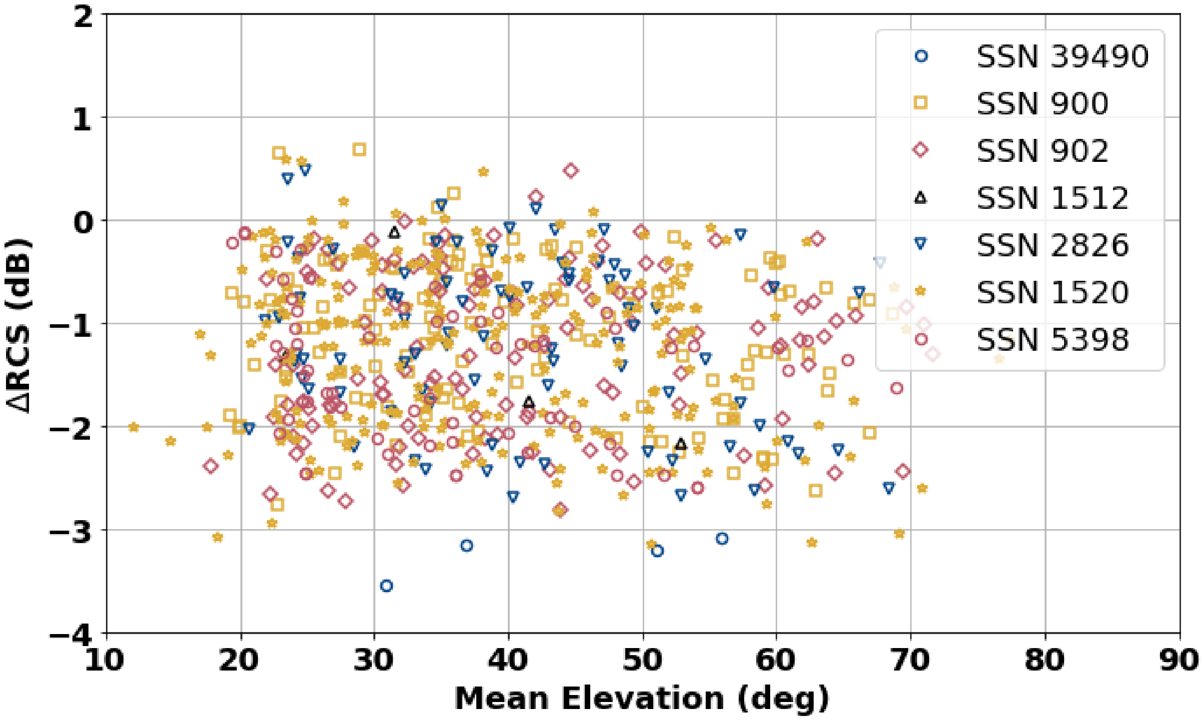

Figure 3-5: ΔRCS versus Elevation for CY2022 with calibration objects identified.

3.4 SPIRAL SCAN CALIBRATION

To calibrate the antenna beam gain pattern, MIT/LL performs spiral scan calibrations before an OD radar data collection period. The spiral scan process involves tracking a calibration object and then performing a slow spiral centered on the object from boresight outward to the edge of the beam in a way that adequately samples the full, 3-dB beamwidth. This data can then be used to fit a beam shape. The beam shape solution currently in use is based on fits to a series of spiral scans from 2017. The beam shape is presumed to be relatively stable over time, though verification of the beam shape stability using the regularly collected spiral scans will be completed at a future date.

Since it is easier to spiral around a stationary point relative to the radar, spiral scans on geosynchronous orbit (GEO) objects are preferable to those on LEO objects. Additionally, over the spiral scan calibration period a 3-axis-stabilized GEO object should provide a constant RCS. Figure 3-6 shows a DRADIS visualization of a spiral scan on a GEO target.

Only the PP channel can be calibrated using the spiral scan method, since both GEO satellites and LEO calibration spheres are used as targets. The OP beam shape is assumed to be the same as the PP beam shape.

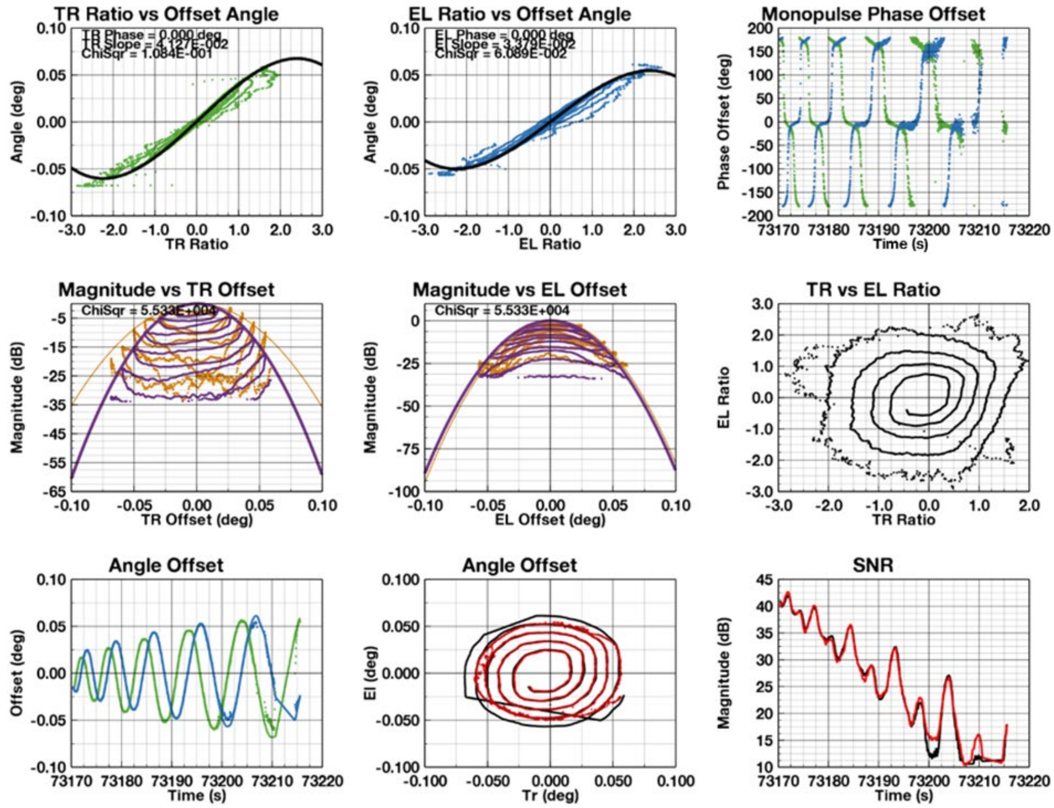

Figure 3-6: Data visualization in DRADIS of a spiral scan on a GEO satellite.

3.5 RADAR CALIBRATION USING NAK COOLANT DROPLETS

The NaK population of debris is an excellent OD radar calibration source shown to have stable count rates as far back as FY 2000 [6]. This liquid, metallic coolant leaked from the ejected cores of the Soviet/Russian Radar Ocean Reconnaissance Satellites (RORSAT) and in microgravity formed into spherical droplets under their own surface tension. Due to the low-velocity separation of these droplets from their parent bodies and the scattering properties of metallic spheres, this population can be separated easily from the rest of the OD population based on altitude, inclination, and polarization.

Figure 3-7 summarizes a model for the cumulative number of NaK particles as a function of the RCS at the HUSIR wavelength of 3 cm (10 GHz). This empirical RCS distribution is based on the work in [7]. The empirical RCS distribution exhibits an inflection point, the location of which is largely independent of the underlying size distribution model [7, 8, 9]. The location of the inflection point at -35 dBsm, indicated by the dashed black lines, is frequency dependent and is related to the RCS associated with the first peak in the Mie resonance regime. Figure 3-8 shows the measured RCS distribution of NaK in CY2022 75E data at 10.1 GHz, which exhibits the expected inflection point. The presence of this inflection point at a value other than -35 dBsm indicates potential calibration issues including, but not limited to, data taken in the rain; hardware calibration errors or digital signal processing timing offsets; and bad sphere-track calibrations.

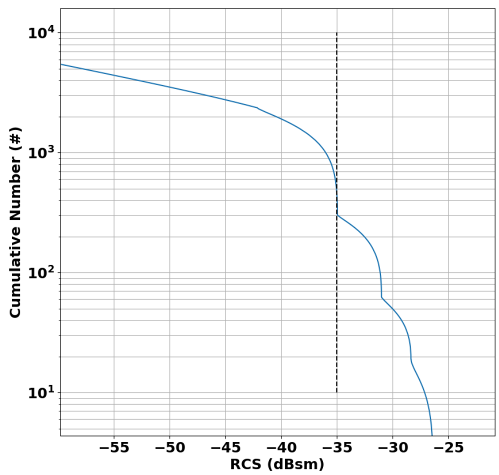

Figure 3-7: Empirical model of NaK RCS distribution.

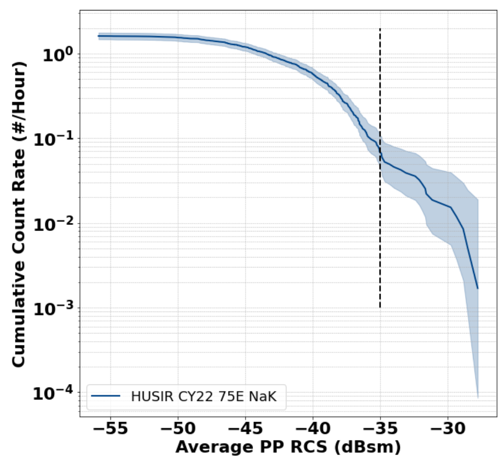

Figure 3-8: RCS distribution of NaK. The shaded regions represent the 2σ uncertainty bounds.

3.6 THE NASA SIZE ESTIMATION MODEL

Size estimates from radar data sources are reported using the NASA SEM, which relates the RCS of debris objects from the measured PP and OP channels and a wavelength to an empirically derived characteristic length. The SEM originated from an early 1990s study led by XonTech that used representative debris objects taken from two U.S. Department of Defense hypervelocity impact tests of satellites conducted at the Arnold Engineering Development Complex [8, 10, 11]. In addition to the representative objects from the impact tests, several debris-like objects were included in the sample to better represent the postulated debris environment at the time. The RCS values for the 39 debris objects were measured at an RCS radar range operated by the System Planning Corporation. RCS measurements of these objects were taken over 4 commonly used radar frequency bands (S band: 2.5647 – 3.9111 GHz; C band: 4.116–7.986 GHz; X band: 8.1544–12.7684 GHz; and Ku band: 12.924 – 17.538 GHz), with 8 frequency samples taken in the lowest frequency band and 16 frequency samples taken in the remaining 3 frequency bands. These radar frequency bands correspond to those used by OD radars. Measurements were taken from multiple orientations of the debris objects to understand the distribution of possible RCS values that each piece of debris would present to a radar as the tumbling debris passes through the radar beam [12, 13, 14].

The characteristic length is the average of the projected dimensions, or the dimensions along the shadow of a debris object. As shown in Figure 3-9, the ODPO defines x as the longest projection dimension, y as the longest shadow dimension in a plane orthogonal to x, and z as the longest projection dimension orthogonal to both x and y [15]. The characteristic length of an object is referred to interchangeably as size or diameter.

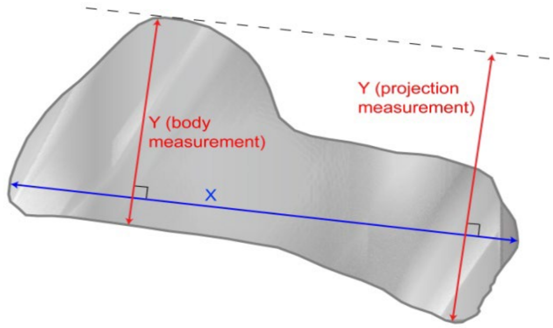

Figure 3-9: Illustration of body and projected measurement on complex shape used in determining characteristic length.

Radar data from sensors operating with different wavelengths may be compared by scaling the size by the wavelength, λ, of the measurement frequency and the RCS by the square of the wavelength. This results in a normalized size, diameter/ λ, and a normalized RCS, RCS/ λ^2. Combining all the measurements – different frequency and object orientations – onto a single plot results in the normalized RCS versus normalized size shown in Figure 3-10. Each of the 2072 data points on this plot is a weighted average for a single debris object over the hundreds of different orientations at a single frequency. The data were weighted to account for the non-uniform sampling of the object orientations during collection.

From the plot shown in Figure 3-10, a scaling curve – the solid black line – was developed, which is the mean of the measured RCS for each normalized size. The solid blue line shows the theoretical RCS for a sphere as a function of size. For debris sizes much smaller or larger than the radar wavelength, the scaling curve approaches the same result as the Rayleigh or optics regions, respectively, for the sphere. Between these two regimes is the Mie resonance region, where for the case of the sphere, there exists a one-to-many mapping between a given RCS value and the size of the sphere. In the case of the size estimation model, however, there is a one-to-one relationship between a given RCS and the size of the object, as shown in Figure 3-10.

For additional details on the piecewise function definition of the SEM or scaling curve from Figure 3-10, see [16].

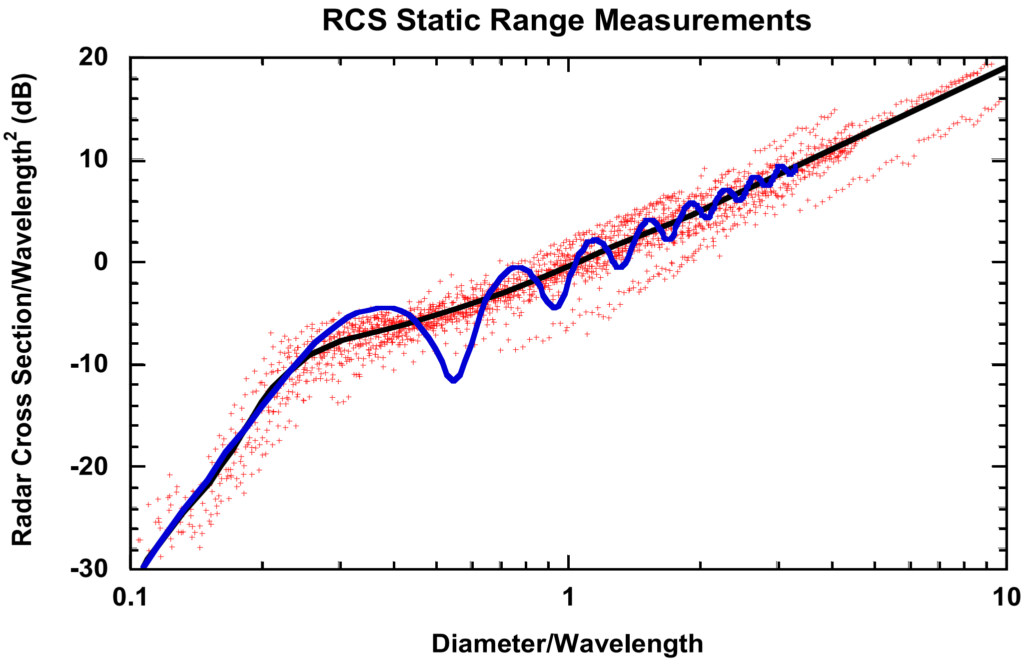

Figure 3-10: Results of RCS-to-size measurements on 39 representative debris objects (red +). The oscillating blue curve is the RCS for a spherical conductor while the smooth black curve is the polynomial fit to the data.

4.0 Results

4.1 DATA COLLECTION OVERVIEW

Most data in CY2022 were collected at 75E. The 75E pointing provides enough Doppler discrimination to estimate some orbital parameters of the detected debris objects, such as inclination calculated by using a circular orbit approximation. In this configuration, detected objects are in orbits with inclination angles having values between the latitude of the radar and the supplementary angle of the latitude. The lower end of the range window in the standard 75E pointing is 415 km, which corresponds to an orbital altitude of 392 km. An augmented 75E, called 75E Low, was implemented briefly near the end of CY2021 and the beginning of CY2022 when the range window was moved 115 km inward, resulting in a minimum range of 300 km, corresponding to an altitude of 281 km. The use of the 75 E Low pointing mode ended in January 2022. The data taken at 75E Low is similar enough to the standard 75E data to present them together in subsequent plots. Differences due to the range window are called out in those subsequent plots. Observations were also performed at 10S and 20S. Although the lower elevation pointing geometries increase the slant range for a given altitude, reducing sensitivity, the lower elevation allows the radar to measure debris in orbits as low as 20° inclination. Table 4-1 shows the minimum and maximum observable ranges and corresponding orbital altitudes for each observation geometry.

Table 4-1. Minimum and Maximum Observable Ranges and Corresponding Orbital Altitudes for Observation Geometry

Pointing	Minimum Range	Maximum Range	Minimum Orbital Altitude	Maximum Orbital Altitude
75E	415 km	2232 km	392 km	2166 km
75E Low	300 km	2117 km	281 km	2053 km
20S	835 km	2654 km	325 km	1321 km
10S	1255 km	3074 km	327 km	1168 km

Table 4-2 shows the number of observation hours at 75E, 75E low, 20S, and 10S pointings and the total number of detections in each configuration. Observation hours represent the total number of hours remaining after the removal of observation windows determined to be contaminated with RFI. The number of detections represents the total number of events for which there were three or more pulses with a single-pulse SNR greater than 5.65 dB, where at least one is in the two-way, 6-dB beamwidth (one-way, two-sided, full-width 3-dB beamwidth). A table showing the total number of hours received from MIT/LL is provided in Appendix A, Table A-1.

Table 4-2: Data Collection Summary Reflecting the Final Curated Data Set for 2022

Pointing	75 E	75 E Low	20S	10S	Total
Hours	278.1	16.5	58.3	64.8	417.7
Detections	4741	371	681	361	6154

4.2 RADAR MEASUREMENTS

This section uses the 75E data as an example to represent the types of information available in the dataset. A comprehensive set of plots for all observation geometries are presented in Appendices C through E. There, range versus range-rate, range versus RCS, altitude versus inclination, cumulative SEM size distributions, cumulative PP SNR distributions, cumulative RCS distributions, and polarization distributions are presented for each pointing direction. Additionally, surface area flux versus altitude and Doppler inclination are presented for the 75E pointing.

4.2.1 Range Versus Range-Rate

Two of the fundamental measurements made by the radar are range and range-rate. Range is the distance from the radar to the target and is calculated from the time it takes the transmitted signal to travel to and return from the target. Range-rate is a measurement of the velocity component of the target along a line connecting the radar to the target and is calculated from the Doppler shift of the received signal. Figure 4-1 presents the range plotted against the range-rate for the 75E data from CY2022. Although detections with range-rates as high as ± 7 km/s are present in the data, most detected objects in the 75E pointing have range-rates between ± 2 km/s, as seen in Figure 4-1. The plot is limited to ± 4 km/s.

The dashed line along the bottom of Figure 4-1 corresponds to the bottom edge of the range window for 75E at 415 km. Since this represents the lowest measurable range, any reflections from objects that are slightly below the range window will have a measured range of 415 km. The few detections below 415 km correspond to data taken at 75E Low.

A cluster of detections near a range-rate of 0.5 km/s and a range of 500 km is highlighted in Figure 4-1 and corresponds to debris from the breakup of the Cosmos 1408 satellite, which occurred as a result of a Russian anti-satellite test on 15 November 2021 [17, 18]. Due to its occurrence late in the CY, this breakup was not yet apparent in regular observation data collected through the end of CY2021 but became evident in the CY2022 data.

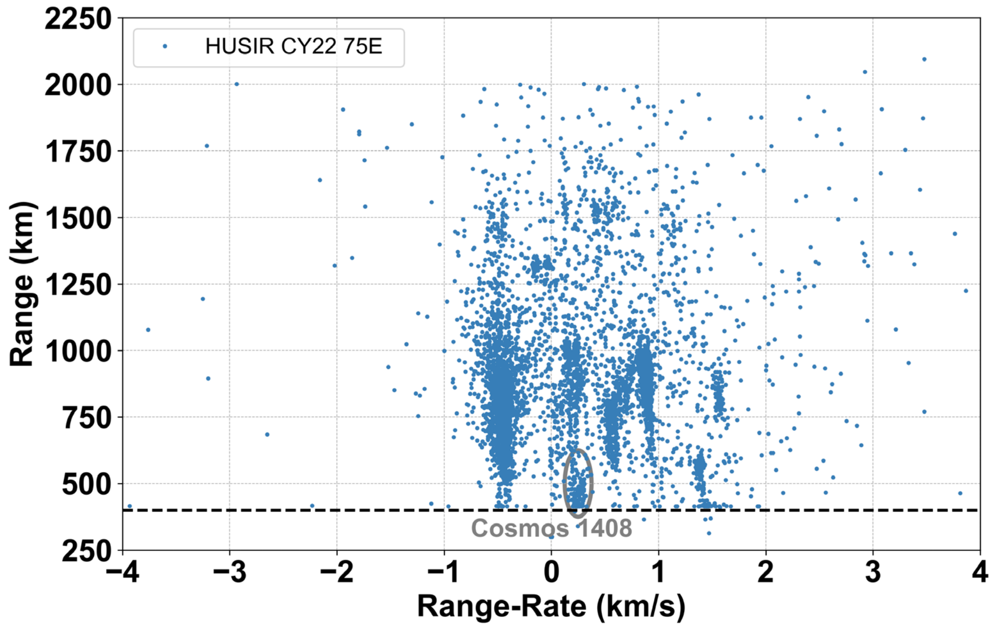

Figure 4-1: Range versus range-rate for the HUSIR 75E data from 2022. The dashed horizontal line corresponds to the bottom edge of the range window for 75E at 415 km.

4.2.2 Altitude Versus Doppler Inclination

An object's inclination and orbital altitude can be estimated, with a circular orbit approximation, using measurements of range and range-rate. All presentations of inclination in this report, unless otherwise indicated, are calculated in this way and are referred to as Doppler inclinations. The 75E observation geometry has been the preferred observation geometry used by the ODPO for many years because it represents a good compromise between having sufficient Doppler discrimination to estimate Doppler inclination for near circular orbits and minimizing loss of sensitivity at a given altitude that occurs for lower-elevation observations [6].

Figure 4-2 shows the altitude versus Doppler inclination for the HUSIR 75E data from CY2022. When represented in this way, distinct families of debris can be isolated and studied independently. The largest of these is composed of heavily trafficked orbits clustered about the black dashed curve that represents the sun-synchronous inclinations for circular orbits. Several notable, historic, on-orbit fragmentation events are also highlighted by black circles, where the center of each circle represents the altitude and inclination of the parent body at the time of the event [17, 18]. A grouping of detections associated with the Starlink constellation at 53°, indicated by the black ellipse, was first seen in HUSIR CY2020 data and has continued to grow in recent years. Additionally, the recent Cosmos 1408 breakup near 500 km altitude and 82° inclination is highlighted. Additional groupings, not labeled, correspond to the NaK family near 65° and a grouping near 900 – 1100 km altitude, 82° inclination that has been identified in previous years and may correspond to a low-velocity shedding event [19]. A family of detections near 45° inclination and 750–900 km altitude has become more noticeable over the past few years and is currently under investigation.

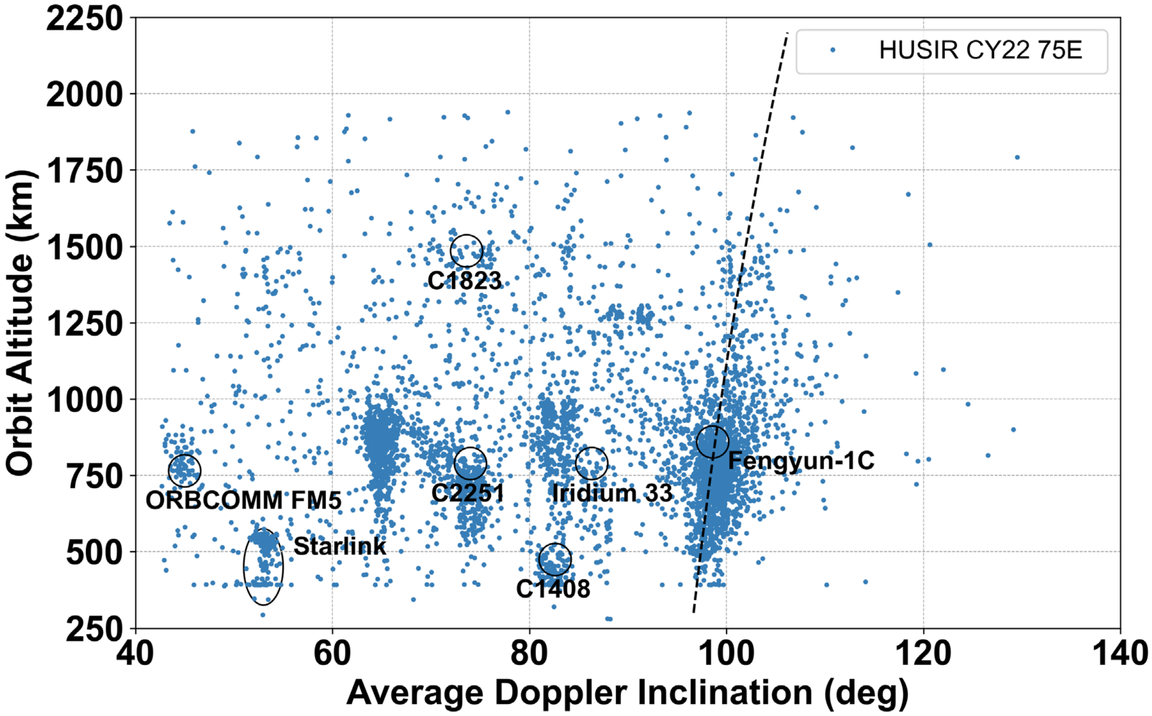

Figure 4-2: Altitude versus Doppler inclination for the HUSIR 75E data from 2022. The black dashed curve that represents the sun-synchronous inclinations for circular orbits.

4.2.3 Range Versus Total RCS

Another key measurement made by the radar, in addition to range and range-rate, is that of RCS. Figure 4-3 shows the range versus total RCS for the HUSIR 75E data in 2022. Additionally, a black dashed line is shown that represents the theoretical RCS of an object with a single-pulse SNR of 5.65 dB as a function of range. This curve is calculated using the average sensitivity of HUSIR for 2022. Figure 4-4 shows the corresponding orbit altitude versus SEM size plot with the corresponding single-pulse SNR curve in this space.

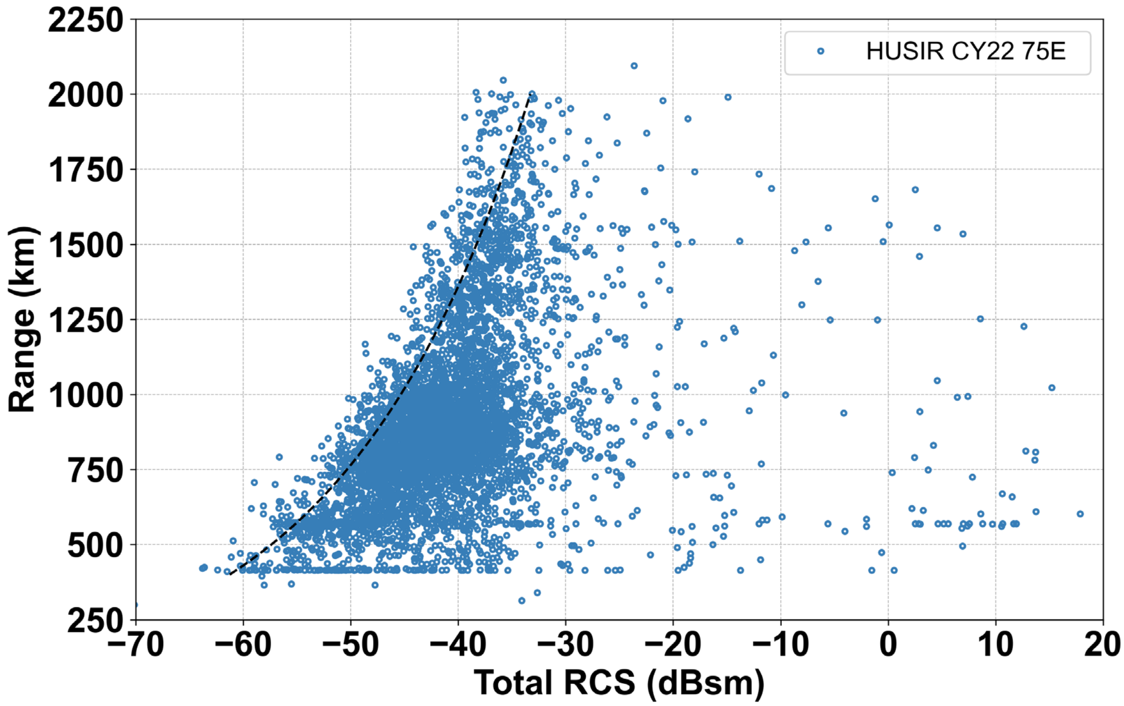

Figure 4-3: Range versus total RCS for the HUSIR 75E data from 2022. The black dashed line represents the range-dependent theoretical RCS of an object with a single-pulse SNR of 5.65 dB.

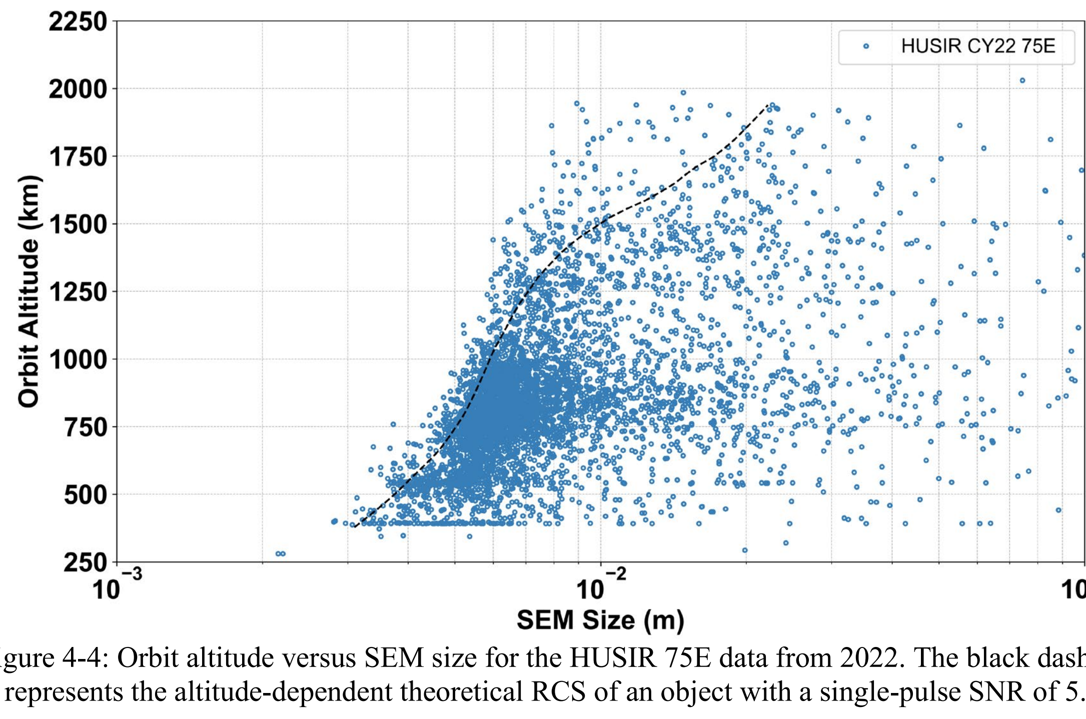

Figure 4-4: Orbit altitude versus SEM size for the HUSIR 75E data from 2022. The black dashed curve represents the altitude-dependent theoretical RCS of an object with a single-pulse SNR of 5.65 dB.

4.2.4 Polarization Distribution

HUSIR transmits right-hand, circularly polarized waveforms and receives both PP- and OP-channel radar returns. The polarization (P) is defined as:

$$P = \frac{RCS_{PP} - RCS_{OP}}{RCS_{PP} + RCS_{OP}}$$

By this definition, the polarization of a perfectly conducting sphere would be + 1. A perfect dipole, with equal values of RCS_{PP} and RCS_{OP}, would have a polarization of zero. Figure 4-5 shows the polarization distribution of the CY2022, 75E data. Additionally, the polarization distribution with detections determined to be NaK removed is shown, illustrating that while the NaK population comprises a large percentage the detections with polarizations near one, there is also a significant portion of non-NaK detections that exhibit positively polarized sphere-like behavior. This could be due to a variety of factors including orientation during detection and material properties.

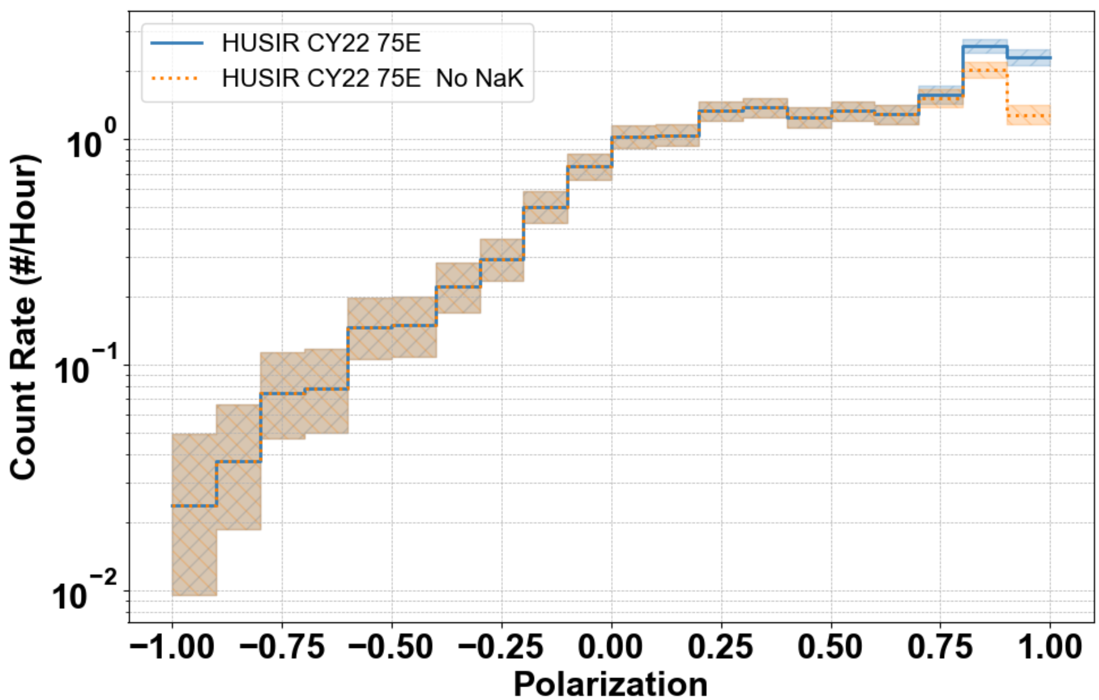

Figure 4-5: Polarization distribution for the HUSIR 75E data from 2022 shown with and without NaK detections (No NaK). The shaded regions represent the 2σ uncertainty bounds.

4.2.5 Comparison of Derived Parameters for Cataloged Objects

When collecting data in beam park mode, some objects cataloged by the SSN pass through the HUSIR field of view. By correlating detections to the SSN catalog, comparisons between the catalog-derived parameters and the HUSIR-derived parameters can help validate measurement results. It must be noted that measurements made to maintain the SSN catalog are performed with different sensors for different purposes. The SSN focuses on obtaining accurate measurements of position and velocity that can be used for orbit determination by tracking objects over time. For OD measurements with HUSIR, the primary goal is to statistically characterize the debris environment to obtain overall distributions of representative sizes and orbits, and the short time arc of an object's path through the beam precludes obtaining precise orbital elements of an individual object.

To correlate detections to the SSN catalog, a two-stage approach is used: a preliminary correlation stage and a second stage, which gathers additional statistics on the preliminary correlation using multiple two-line element sets (TLEs). The first stage reviews each detection and checks for a correlation with each object in the SSN catalog. It pulls the closest TLE in time to the detection for each object, propagates the TLE to the time of detection, and computes the predicted range, range-rate, AZ offset, and EL offset expected at that time. If the difference in the TLE-predicted values relative to the measured values are within a certain tolerance, a correlation is declared. The tolerances used for CY2022 were ± 2 km in range, ± 200 m/s in range-rate, and ± 2° in AZ and EL.

In the second stage, each candidate correlation identified in the first stage is reviewed using all available TLEs for the object in a ± 5-day period. To account for potential timing errors, the TLEs are propagated to the time of closest approach to the boresight of the radar, as predicted by the individual TLE, rather than the time of detection measured by the radar. Once all TLEs have been propagated to their respective times of closest approach, statistics on the minimum, maximum, and mean predicted parameters are gathered. The detection list contains fields indicating whether the correlation was within the uncertainties in AZ, EL, range, and range-rate that are added as part of the second stage of the correlation process.

Comparisons of the HUSIR-derived size and SSN-reported size for HUSIR 75E detections collected in CY2022 that correlate to cataloged breakup and anomalous debris, as defined in [17], are shown in Figure 4-6. Correlations to intact objects are not shown in this figure as the SEM was developed for breakup fragments which are in general irregular in shape. The main lobe detections roughly follow the one-to-one dashed line, indicating a general agreement in measured sizes. Three additional lines that correspond to the first (- 41 dB), second (- 49 dB), and third (- 55 dB) sidelobes of HUSIR also are shown. The measured RCS from different sensors can vary based on the aspect angle presented to the radar at the time of measurement and the RCS history measured by the SSN. In general, if a detection is near the one-to-one line, it is well above the sidelobe levels and classified as a main lobe detection. For main lobe detections, the two data sources agree for larger objects. For small objects, sizes calculated by HUSIR are typically smaller than those calculated by the SSN. This is consistent with previous results in [6] where it was concluded that some SSN sensors historically overestimated the size of smaller debris fragments due to how they estimated average RCS from multiple pulses.

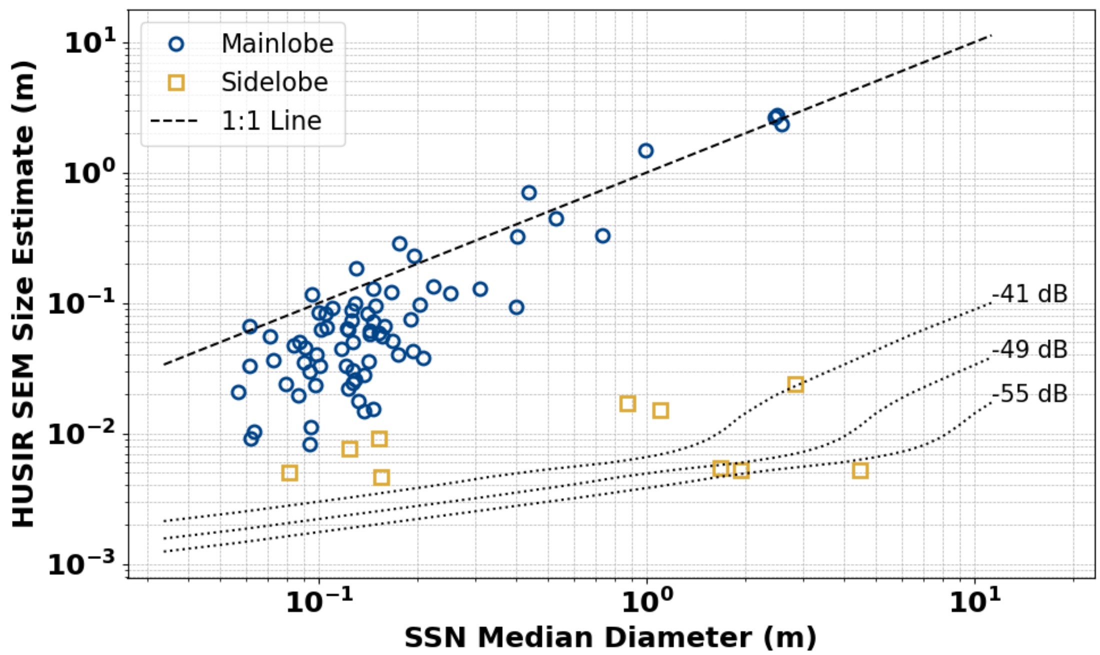

Figure 4-6: Comparison of the HUSIR-derived size and SSN-reported size for HUSIR 75E detections collected in CY2022 with the 10.1 GHz waveform that correlate to cataloged breakup and anomalous debris. The dotted curves at -41 dB, -49 dB, and -55 dB represent HUSIR's first, second, and third sidelobes, respectively.

Figure 4-7 compares the Doppler inclination derived from HUSIR data of main lobe detections with the cataloged inclination for correlated targets in the CY2022, 75E data. Most points lie on or near the dashed line that represents a one-to-one match of the SSN catalog inclination values and the Doppler inclination values. Much of the departure from the one-to-one line seen in Figure 4-7 is due to the Doppler inclination calculation, *i.e.*, approximating the objects as having a circular orbit. Figure 4-8 shows the SSN eccentricity versus the difference between the SSN inclination and HUSIR Doppler inclination. For eccentricities near zero, the differences are within +/- 3 degrees while the difference increases as eccentricity increases.

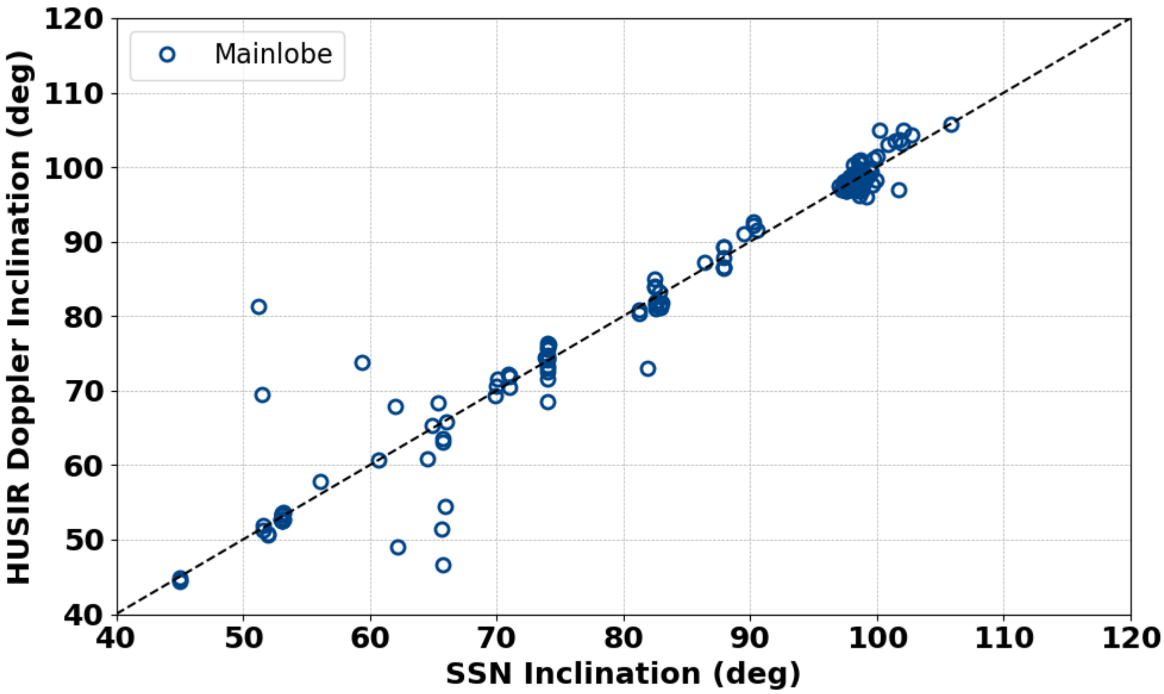

Figure 4-7: Comparison of the Doppler inclination derived from HUSIR data with the cataloged inclination for correlated targets in the CY2022 75E data.

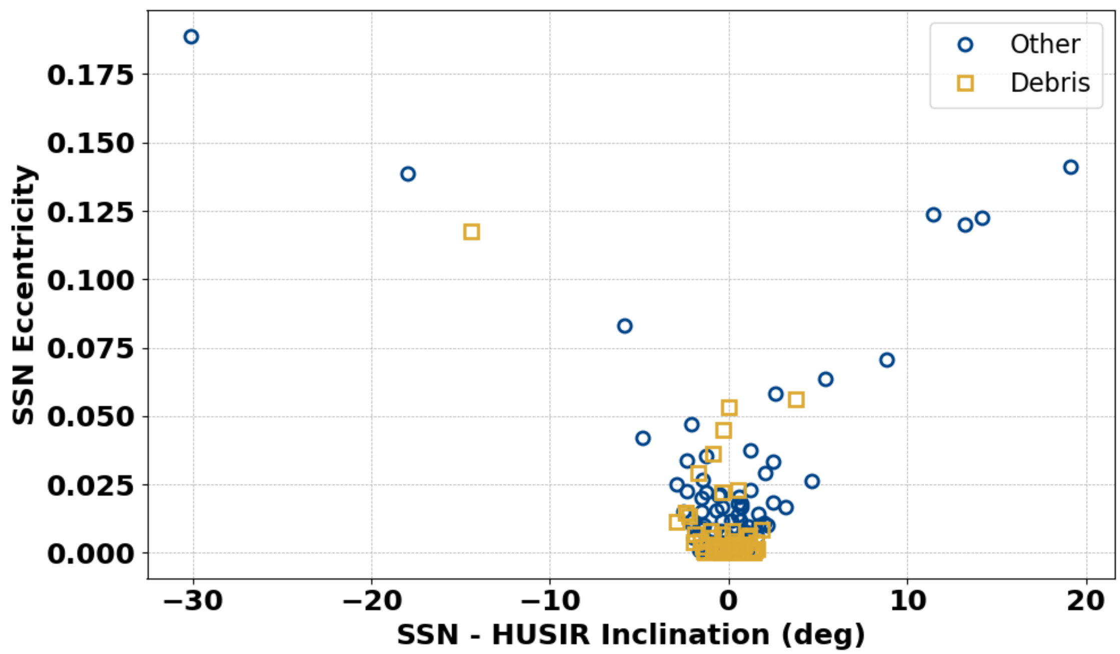

Figure 4-8: SSN eccentricity versus the difference between cataloged (SSN) inclination and Doppler inclination derived from HUSIR data.

4.3 ENVIRONMENT CHARACTERIZATION SUMMARY

The radar data presented here provides a broad overview of the state of the debris environment in LEO. Since the radar sensitivity changes from year-to-year, flux charts in this section, which compare multiple years of data, are typically presented with the flux down to a limiting size and an upper bound on altitude. Each subsection will compare the CY2022, 10.1 GHz data to CY2021 and CY2020 datasets, which combine 10 GHz and 10.1 GHz, to identify new features in the data or the environment. As discussed in section 2.0, the 10 GHz and 10.1 GHz data are comparable.

4.3.1 SEM-size Cumulative Distribution

While the total count rate of debris can change each year due to changes in radar sensitivity, the distributions of these measured sizes should remain largely the same. Any large changes from year-to-year indicate a significant change in the OD environment. Figure 4-9 compares the cumulative size distributions for the CY2020, CY2021, and CY2022, 75E datasets, limited to detections with an SEM-size greater than 10 cm. The shaded regions represent the 2σ-Poisson uncertainties. Cumulative count rates are comparable in both datasets. Changes in the environment that are localized in altitude and inclination can be masked when aggregating all detections into a single cumulative count rate. It is, therefore, of interest to compare flux distributions in altitude and inclination as well.

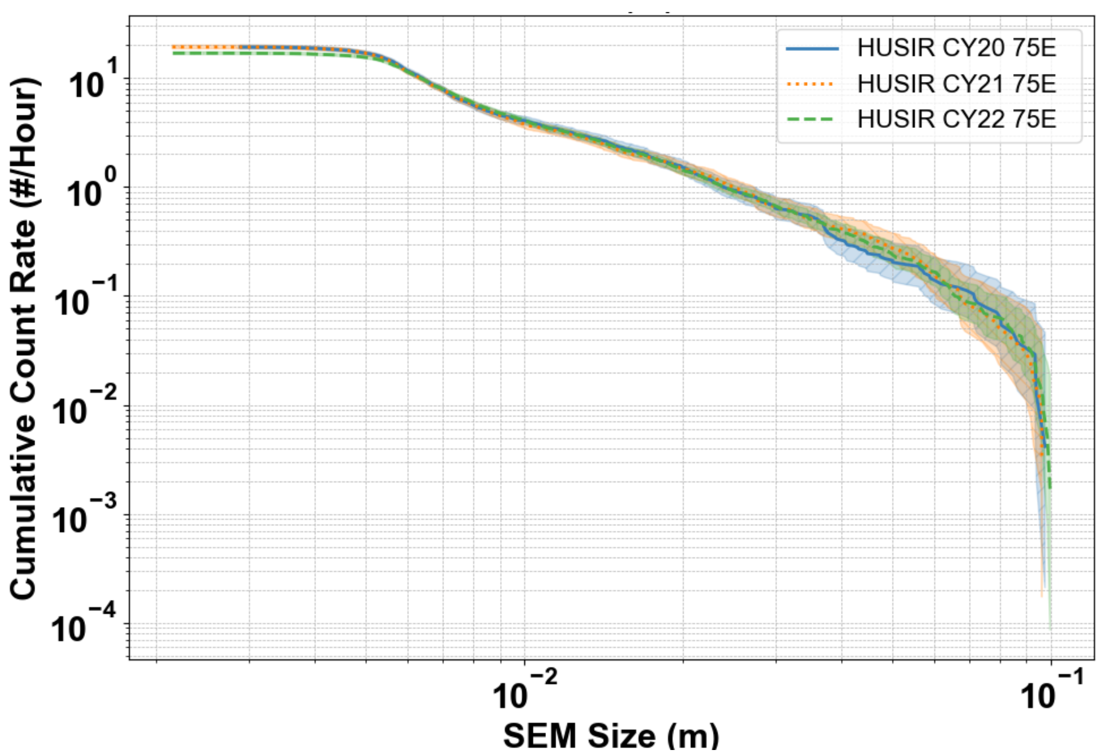

Figure 4-9: SEM-size cumulative distribution for all 75E data, by year, limited to detections with an SEM-size less than 10 cm. The shaded regions represent the 2σ uncertainty bounds.

4.3.2 Flux Versus Altitude

Surface area flux is defined as the number of detections through the lateral surface area of the radar beam, considering the 3 dB beamwidth of the main beam only, within a given period. Total flux is the flux of all objects regardless of size, where size is estimated using the NASA SEM, as described in Section 3.6. To aid in comparing different years, surface area flux to a limiting size is shown. This represents the flux of objects with a size equal to or greater than the chosen limiting size. Here, surface area flux is presented to limiting sizes of 7.2 mm and 2.4 cm, depending on altitude. These correspond to the 99% completeness sizes at 1000 km and 1600 km altitude. Details of the estimation are presented in Appendix B.

Figure 4-10 shows the surface area flux versus altitude limited to 7.2 mm for all 75E observations, by year, with 50 km bins. There is a trend of increasing flux in the 500 – 550 km altitude bin. While from one year to the next, the confidence intervals overlap, when comparing CY2022 to CY2020 a statistically significant increase can be seen, likely attributable to increased Starlink traffic. A similar trend is present in the 400 – 500 km altitude bins, likely due to the Cosmos 1408 breakup, where there is little to no overlap between the CY2020 and CY2022 confidence intervals. There is also evidence of an increase in the 800 – 850 km altitude bin from CY2020 to CY2022 that merits continued observation and analysis. Figure 4-11 shows the surface area flux versus altitude limited to 2.4 cm for all 75E observations, by year, with 50 km bins. The shaded regions represent the 2σ-Poisson uncertainties. The same statistically significant increase from CY2020 to CY2022 can be seen in the 500 – 550 km altitude bin even at this larger limiting size.

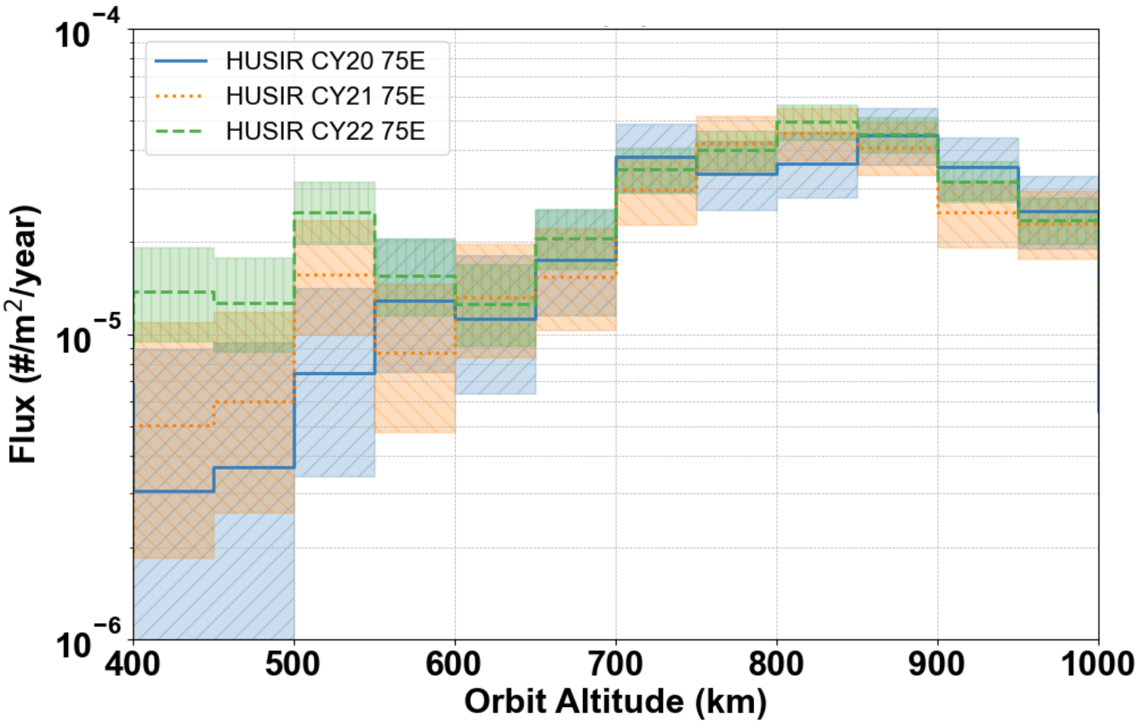

Figure 4-10: Surface area flux versus altitude limited to 7.2 mm for all 75E data, by year. The shaded regions represent the 2σ uncertainty bounds.

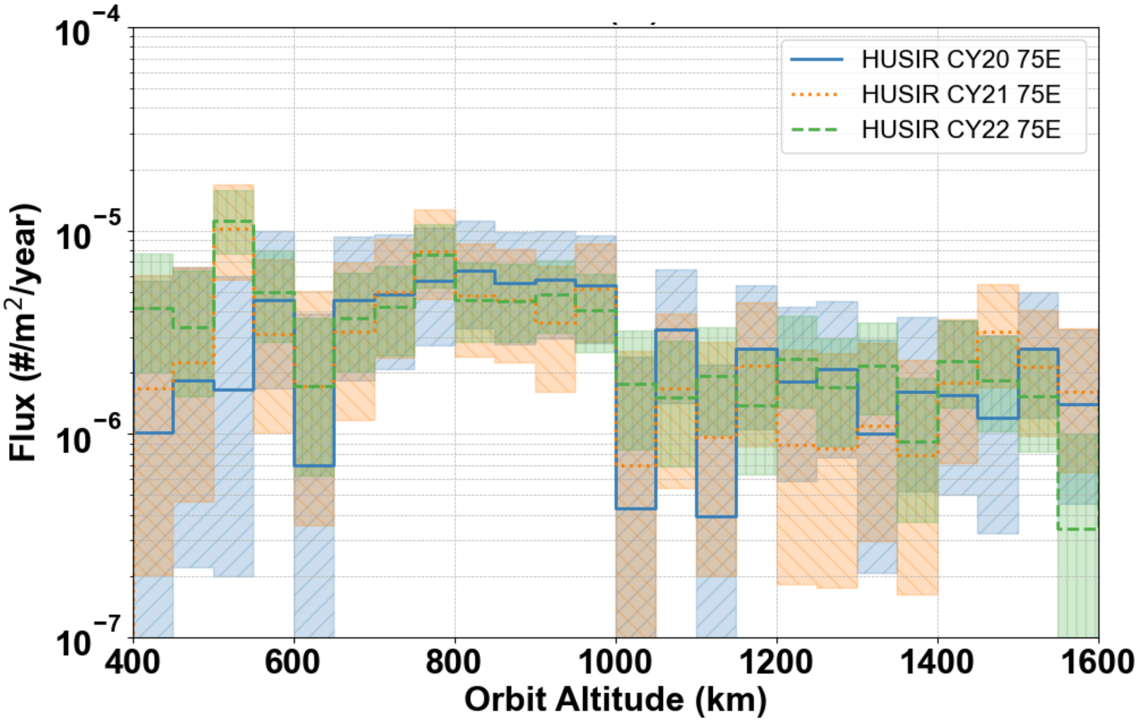

Figure 4-11: Surface area flux versus altitude limited to 2.4 cm for all 75E data, by year. The shaded regions represent the 2σ uncertainty bounds.

4.3.3 Flux Versus Inclination

In addition to flux versus altitude, examining flux versus inclination gives more insight on the distinct populations and families of debris. Flux is defined as in previous sections, except that the beam area is the total surface area of the beam from the minimum observable altitude to the maximum observable altitude, since objects observed at a particular inclination can be at any observable altitude in the 75E geometry. The fluxes presented in this section are to limiting sizes of 7.2 mm and 2.4 cm.

Figure 4-12 shows surface area flux versus inclination limited to sizes larger than 7.2 mm and altitudes below 1000 km for all 75E data, by year, using 2°-wide bins. Again, while the confidence intervals of adjacent years overlap, there is a clear increasing trend of flux in the 52° – 54° inclination bin with a statistically significant increase from CY2020 to CY2022. This, like the trend in the 500 – 550 km altitude bin, is related to increased Starlink traffic. There is also an increase in the 80° – 84° bins (reaching statistical significance in the 80° – 82° bin), attributable to the Cosmos 1408 breakup. Figure 4-13 shows surface area flux versus inclination limited to sizes larger than 2.4 cm and altitudes below 1600 km for all 75E data, by year, with 5°-wide bins. Trends of increasing flux related to Starlink and Cosmos 1408 are present, but with confidence intervals still overlapping due to lower counts at the larger limiting size and inclusion of detections from altitudes much higher than the Cosmos 1408 breakup and Starlink orbits.

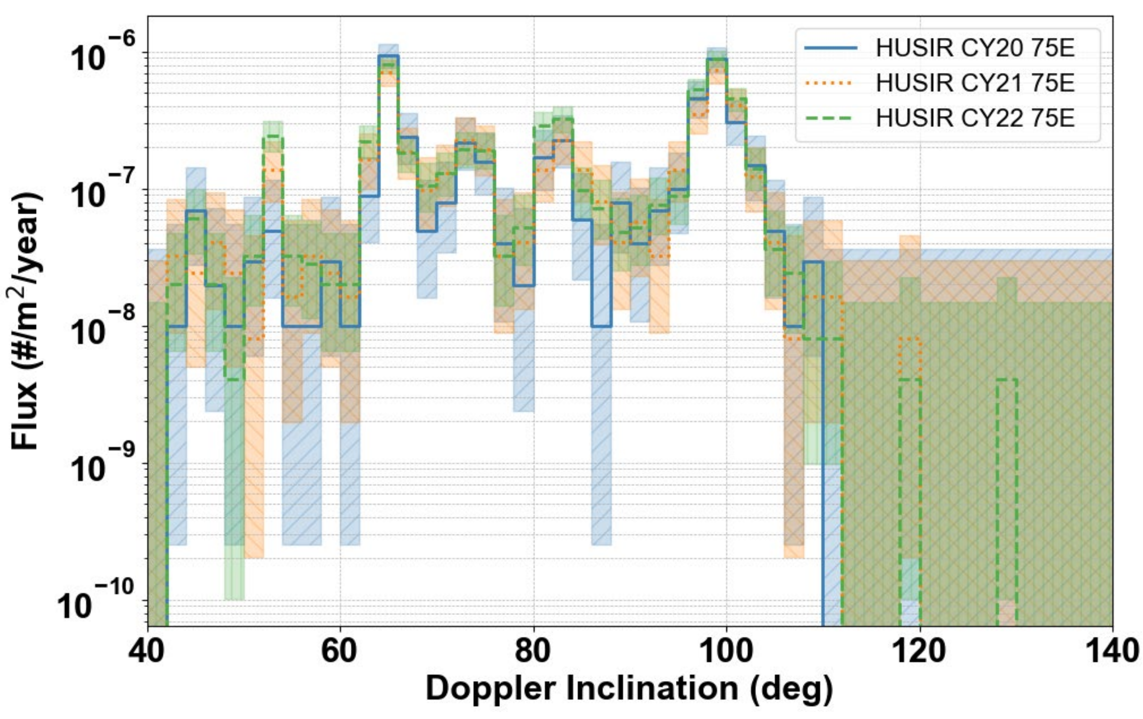

Figure 4-12: Surface area flux versus inclination limited to sizes larger than 7.2 mm and altitudes below 1000 km for all 75E data, by year, with 2°-wide bins. The shaded regions represent the 2σ uncertainty bounds.

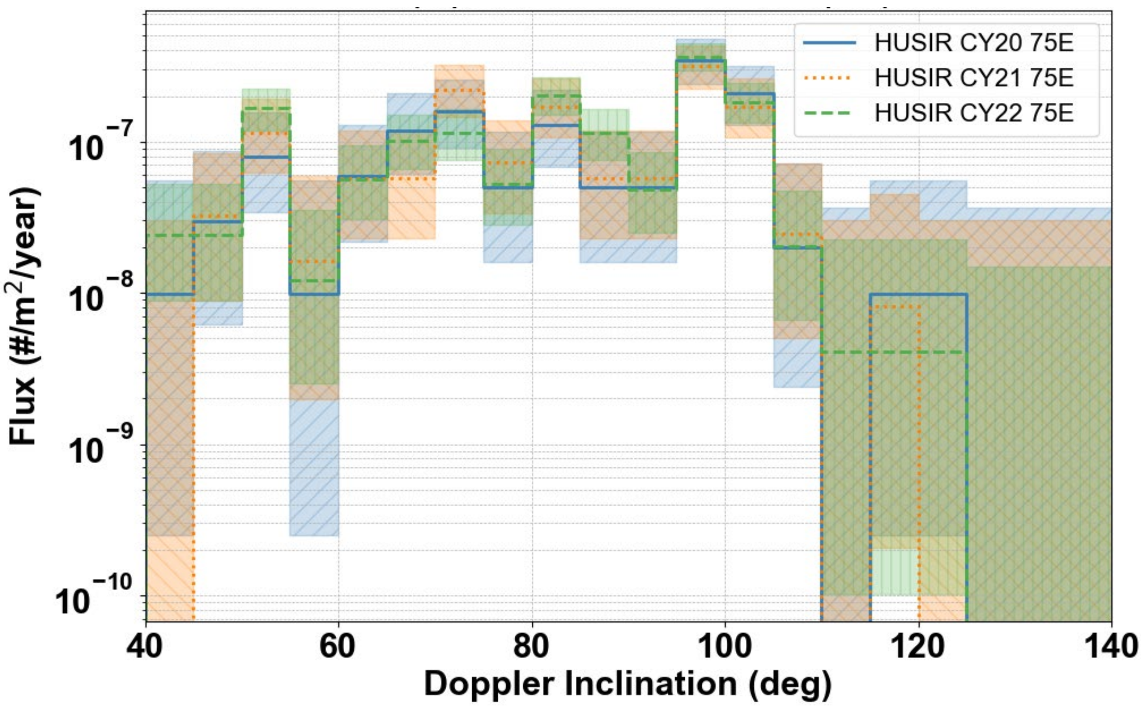

Figure 4-13: Surface area flux versus inclination limited to sizes larger than 2.4 cm and altitudes below 1600 km for all 75E data, by year, with 5°-wide bins. The shaded regions represent the 2σ uncertainty bounds.

4.4 HUSIR OBSERVATIONS VS ORDEM 3.2 PREDICTIONS

In addition to comparisons against data from previous years, it is also informative to compare data against model predictions. This serves to validate model predictions as well as offer insights into model improvements that can be made in the future. In this section, HUSIR CY2022 data is compared against the NASA Orbital Debris Engineering Model (ORDEM) 3.2 to assess the current environment against model expectations. ORDEM 3.2 was updated in March 2022 to include fragments from the Cosmos 1408 breakup [20], thus data from CY2022 provides the first opportunity to compare the updated model against the regular statistical HUSIR measurements including these fragments.

Comparisons are made between the surface area flux distribution as a function of altitude and the cumulative flux distribution as a function of SEM-size for specific altitudes of interest. Note that the sizes reported here from ORDEM have been calculated by converting the intrinsic, physical debris sizes from the model to an RCS distribution, then converting to an SEM size, as discussed in section 2.2.5 of [21]. This method accounts for the uncertainties in the RCS-to-SEM-size conversion and provides a more consistent metric for comparison between the model and data. In addition, the contribution from the NaK subpopulation has been removed from the ORDEM fluxes, and likewise detections corresponding to an NaK filter have been removed from the HUSIR data.

The surface area flux distribution as a function of altitude for both the HUSIR data and

ORDEM 3.2 model predictions is shown in Figure 4-14. As a baseline comparison, the ORDEM 3.1 flux is also included. The ORDEM 3.2 update incorporated fragments from the Cosmos 1408 breakup; otherwise, the populations in ORDEM 3.2 remained unchanged from ORDEM 3.1. The shaded blue region represents Poisson 2σ uncertainties in the measured HUSIR flux. The comparison is limited to OD with SEM-sizes between 7.2 mm, the 99% completeness limit of HUSIR CY2022 data (see Section 2.1), and 10 cm. The upper size limit is imposed to remove the effect of larger objects likely included in the SSN catalog.

In addition, detections attributable to the Starlink constellation have been removed from the HUSIR data. The Starlink constellation is not resident in the ORDEM 3.2 model, as the spacecraft were not part of the background launch traffic at the time the underlying ORDEM 3.1 model populations were developed. Thus, their contribution to the HUSIR flux has been filtered out to enable a better comparison of the model and the data. Specifically, detections correlated to Starlink spacecraft as well as detections with altitudes and inclinations of 400 – 550 km and 52° – 55° or 400 – 535 km and 42° – 44°. The minimum altitude of 400 km captures those spacecraft that may have been in transit to their operational orbits at the time of detection.

For this size range, the ORDEM 3.2 predictions of 400 – 650 km are significantly higher than the HUSIR flux, well outside the uncertainty bounds. This is due to the Cosmos 1408 breakup cloud, which dominates the flux in the 400 – 500 km altitude range and contributes to the flux at surrounding altitudes. This is evident by comparing the ORDEM 3.2 flux to that of ORDEM 3.1. The difference between the ORDEM 3.2 prediction and the HUSIR CY22 data is attributed to recent solar flux activity being higher than that predicted at the time ORDEM 3.2 was developed, causing the Cosmos 1408 fragments to decay faster than originally modeled [22].

Figure 4-15 shows the cumulative flux distribution as a function of SEM-size for altitudes below 1000 km, comparing the HUSIR data and ORDEM 3.2 predictions. As in Figure 4-14, for better comparison with the model, detections attributable to the Starlink constellation have been removed from the HUSIR data, specifically detections correlated to Starlink spacecraft as well as detections with altitudes and inclinations of 400 – 550 km and 52° – 55° or 400 – 535 km and 42° – 44°. There are several regions where the HUSIR measurements deviate from the ORDEM 3.2 predictions. For SEM-sizes greater than approximately 5 cm, there is an apparent increase in the observed flux relative to the ORDEM 3.2 prediction. A similar increase was seen in CY2018 [23]. As in that year, the number of objects with an SEM-size greater than 1 m detected in CY2022 is significantly higher than in previous years: 31 objects not attributable to a Starlink spacecraft (either by correlation or per the altitude and inclination limits listed above) were detected in 2022 as compared to 3 in 2021, 8 in 2020, and 7 in 2019. This increase in the number of detections of larger objects will continue to be monitored.

Looking at the cumulative flux over all sizes, the higher ORDEM 3.2 flux from approximately 8 mm to 2 cm is likely due to the higher flux from Cosmos 1408 fragments in the model, as discussed above. Below approximately 7 mm to 8 mm, the slightly higher slope in the HUSIR data has also been observed in previous years and is attributable to a signal processing change made in 2018 leading to a more accurate distribution of sizes for low- to medium-SNR detections [24, 3]. The underlying ORDEM 3.2 populations, aside from the inclusion of the Cosmos 1408 fragments, were built using data from before this signal processing change was made, thus the behavior of this comparison is like previous comparisons with ORDEM 3.1. Since the 99% data completeness limit for CY2022 is 7.2 mm, the most applicable data-model comparisons are for sizes larger than this limit.

ORDEM is updated periodically to reflect the newest available data and the dynamic behavior of the OD environment. The evolution of the Cosmos 1408 and other debris clouds, based on updated solar cycle predictions, as well as changes in launch behavior, such as for the Starlink and other constellations, will be incorporated in upcoming ORDEM releases.

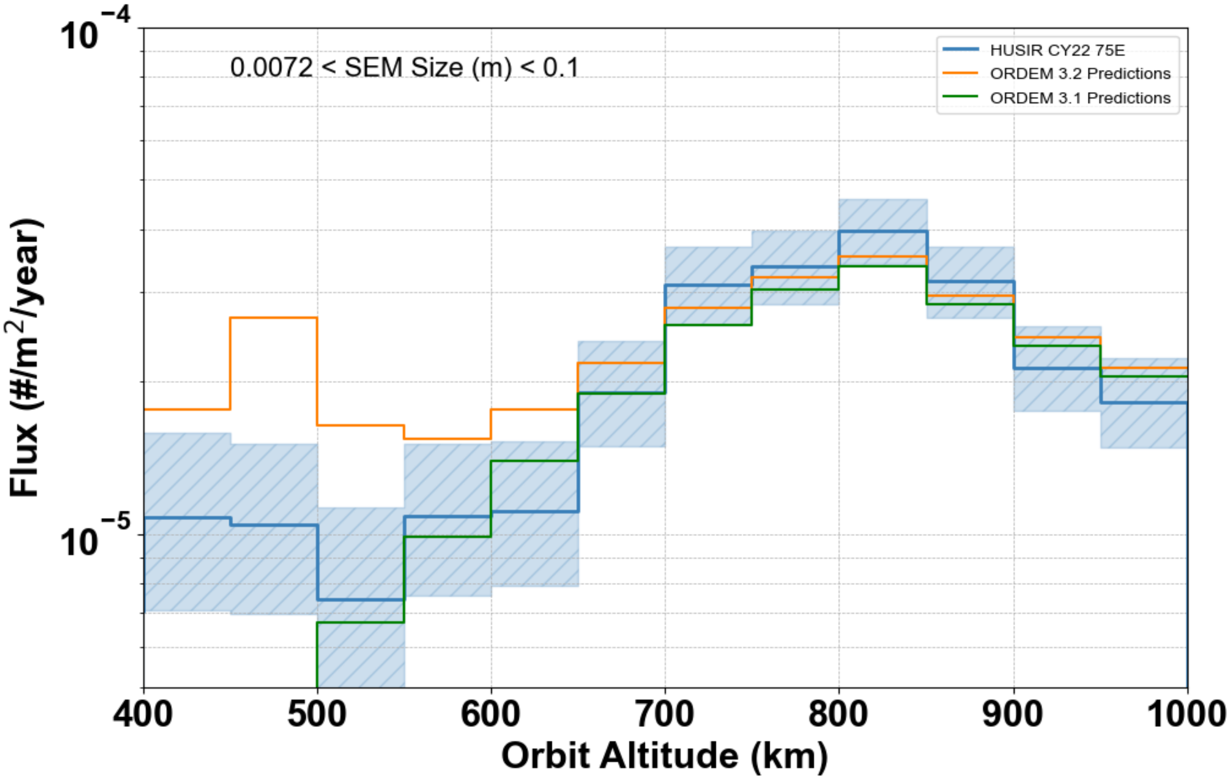

Figure 4-14: Surface area flux versus SEM size comparing HUSIR CY2022 data to ORDEM 3.2 predictions for SEM sizes between 7.2 mm and 10 cm. Detections attributable to Starlink satellites, specifically correlated Starlink detections and those having an altitude of 400 – 550 km and inclination of 52° – 55° or 400 – 535 km and 42° – 44°, have been removed from the HUSIR data. The shaded blue region represents Poisson 2σ uncertainties in the HUSIR data.

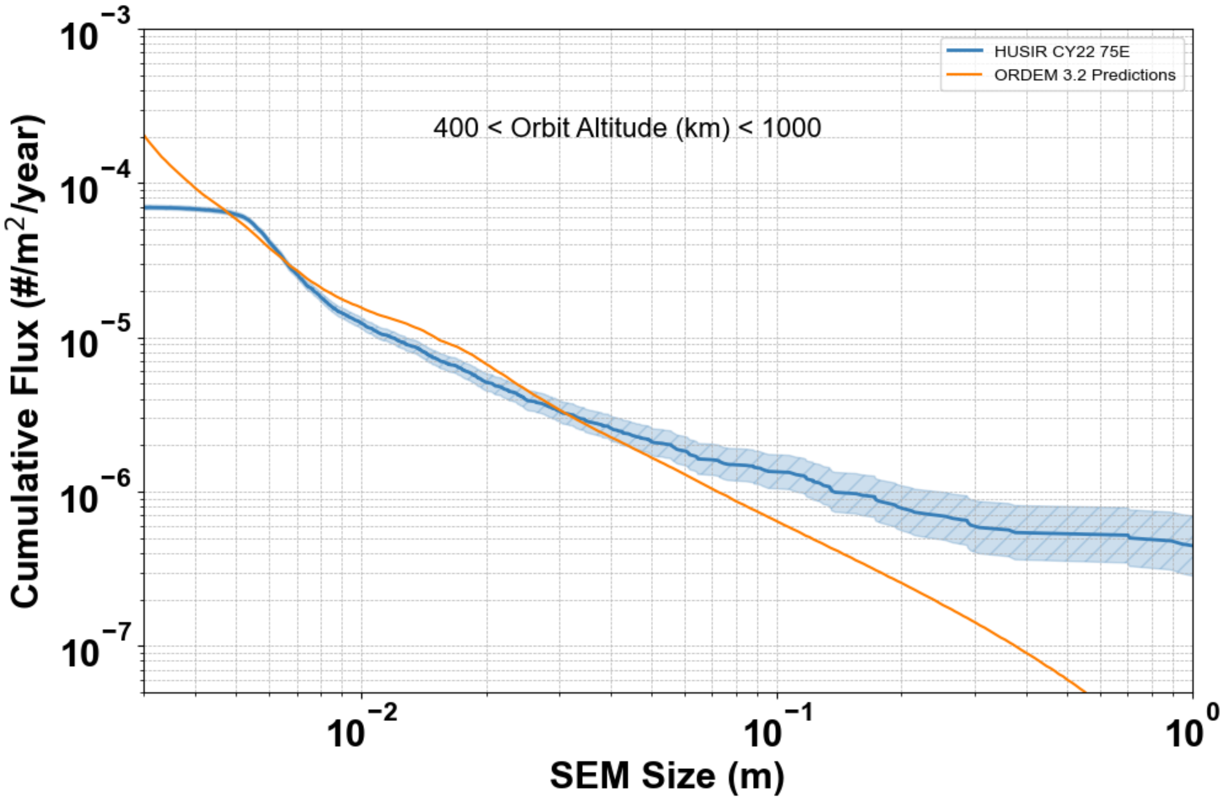

Figure 4-15: Cumulative flux versus SEM size comparing HUSIR CY2022 data to ORDEM 3.2 predictions for altitudes between 400 km and 1000 km. Detections attributable to the Starlink constellation, specifically correlated Starlink detections and those having an altitude of 400 – 550 km and inclination of 52° – 55° or 400 km-535 km and 42° – 44°, have been excluded from the HUSIR data. The shaded blue region represents Poisson 2σ uncertainties in the HUSIR data.

5.0 Summary

The LEO environment as observed by HUSIR in CY2022 and measurements from the radar were discussed and analyzed. A total of 420.4 observation hours were processed and analyzed from HUSIR at 75E-, 75E Low-, 20S-, and 10S-pointing geometries. Approximately 418 hours met requirements for analysis. Detected objects were measured for RCS, range, range-rate, and polarization. This data was analyzed to produce orbital altitude and inclination, size, and flux distributions.

The exclusive use of the 10.1 GHz NWF starting in CY2021 Q4 to mitigate RFI was discussed. As the NWF was previously shown to produce data comparable to the 10 GHz waveform [2], all CY2020 and CY2021 measurements presented for comparison with CY2022 consisted of a combined dataset using both the 10 GHz waveform and 10.1 GHz NWF.

Cumulative size distributions for CY2020, CY2021, and CY2022 were compared. These comparisons between years provide a broad overview of the state of the OD environment in LEO. Cumulative count rates were comparable across all datasets down to a limiting size. Surface area flux versus altitude and surface area flux versus inclination for CY2020, CY2021, and CY2022 were also compared. The CY2022 flux was elevated slightly above the CY2021 flux from 600 km altitude down to at least 400 km altitude, approximately the lowest measurable altitude by HUSIR's standard 75E pointing; this altitude range corresponds to the altitudes of the Starlink constellation and the Cosmos 1408 breakup event. When comparing to CY2020 data, trend of increasing flux is present at these altitudes with statistically significant increases in the 400 – 450 km and 500-550 km altitude bins. The CY2022 flux was slightly elevated above CY2021 levels from 52° to 54° and from 80° to 82° Doppler inclination, corresponding to the inclinations of the Starlink constellation and the Cosmos 1408 breakup, respectively. Comparisons to CY2020 showed a trend of increasing flux in these inclinations bins as well, with the 52° – 54° and 80° – 82° inclinations bins reaching statistical significance.

This report presented key results from the curated CY2022 HUSIR radar measurements of the OD environment. HUSIR data has been the primary source of information for the development of NASA's OD models down to approximately 5 mm in LEO. Continued monitoring of the environment in the size ranges efficiently measured by HUSIR is needed to continue updating, validating, and refining these models.

(This page left intentionally blank)

6.0 References

1. Stansbery, E., *et al*. “Characterization of the Orbital Debris Environment Using the Haystack Radar,” *JSC-32213*, NASA/JSC, Houston, TX (1993).
2. Murray, J. and Matney, M. “Haystack Ultra-Wideband Satellite Imaging Radar Measurements of the Orbital Debris Environment: 2021,” *NASA/TP-20230008344*, NASA/JSC, Houston, TX (2023).
3. Murray, J. and Kennedy, T. “Haystack Ultra-Wideband Satellite Imaging Radar Measurements of the Orbital Debris Environment: 2020,” *NASA/TP-20220006634*, NASA/JSC, Houston, TX (2022).
4. Matney, M., *et al*. "The NaK Population: A 2019 Status," *First International Orbital Debris Conference,* Sugar Land, TX, (2019).
5. Murray, J., *et al*. “Haystack Ultra-Wideband Satellite Imaging Radar Measurements of the Orbital Debris Environment: 2014-2017,” *NASA/TP-2019-220302*, NASA/JSC, Houston, TX (2019).
6. Stokely, C., J. *et al*. “Haystack and HAX Radar Measurements of the Orbital Debris Environment; 2003,” *JSC-62815*, NASA/JSC, Houston, TX (2006).
7. Foster, J., *et al*. "NaK Droplet Source Modeling." *54th International Astronautical Congress,* Bremen, Germany, (2003).
8. Bohannon, G., Dalquist, C., and Pardee, M. "Physical Descriptions of Debris Objects Used in Static RCS Measurements," *XonTech Report 910555-1978* (1991).
9. Krisko, P., and Foster, J. "Modeling the sodium potassium droplet interactions with the low earth orbit space environment," *Acta Astronautica,* vol. 60, pp. 939-945 (2007).
10. Stansbery, E., *et al*. “Characterization of the Orbital Debris Environment using the Haystack Radar, Appendix A,” *JSC-32213*, NASA/JSC, Houston, TX (1993).
11. Bohannon, G., Caampued, T. and Young, N. "First Order RCS Statistics of Hypervelocity Impact Fragments," *XonTech Report 940128-BE-2305*, (1994).
12. Barton, D., *et al*. “Final Report of the Haystack Orbital Debris Data Review Panel,” *Technical Memorandum 4809 NASA/TP-2004-0200965*, NASA/JSC, Houston, Texas (1998).
13. Everett, R., Caampued, T., Chu, J., and Bohannon, G. "Summary of Data Processing of September 1990 SPC Debris Data," *XonTech Report 910147-1937* (1991a).
14. Everett, R., Dalquist, C., Caampued, T., and Bohnnon, G. "Summary of Processing of January 1991 SPC Debris Data," *XonTech Report 910383-1965* (1991b).
15. Hill, N. "Measurement Techniques for Hypervelocity Impact Test Fragments," *59th International Astronautical Congress,* Glasgow, Scotland (2008).
16. Xu, Y., *et al.* "A Statistical Size Estimation Model for Haystack and HAX Radar Detections," *56th International Astronautical Congress,* Fukuoka, Japan, (2005).
17. Anz-Meador, P., Opiela, J. and Liou, J.-C. “History of On-Orbit Satellite Fragmentations, 16th Edition,” *NASA/TP-20220019160*, NASA/JSC (2022).
18. ODQN vol. 26, issue 1, pp. 1-5. "The Intentional Destruction of Cosmos 1408." *Orbital Debris Quarterly News* 26 (1): 1-5, (2022).
19. Gates, D., and Anz-Meador, P. "An 82 Degree Inclination Cloud Revealed by Radar." *First International Orbital Debris Conference.* Sugarland, TX, (2019).
20. ODQN vol. 26, issue 1, p. 5. "Orbital Debris Engineering Model 3.2 Release." *Orbital Debris Quarterly News* 26 (1): 5, (2022).

21. Kennedy, T., Matney, M., Cowardin, H., Manis, A., Vavrin, A., Seago, J., Gates, D., Anz-Meador, P., and Xu, Y. *NASA Orbital Debris Engineering Model (ORDEM) 3.1: Model Verification and Validation.* NASA/TP-20220002309, (2022).
22. ODQN vol. 28, issue 2, pp. 2-4. "Evolution of the Cosmos 1408 Breakup Cloud: A Two-Year Status." *Orbital Debris Quarterly News* 2-4 (2024).
23. Murray, J., and Kennedy, T. "Haystack Ultra-Wideband Satellite Imaging Radar Measurements of the Orbital Debris Environment: 2018," Houston: NASA/JSC (2020).
24. Murray, J., and Kennedy, T. "Haystack Ultra-Wideband Satellite Imaging Radar Measurements of the Orbital Debris Environment: 2019," Houston: NASA/JSC (2021).

Appendix A: Total Number of Hours Received from MIT/LL

Table A-1: Data Collection Summary Reflecting the Total Number of Observation Hours Received from MIT/LL in CY2022

10.1 GHz Waveform	75E	75 E Low	20S	10S	Total
	Hours	Hours	Hours	Hours	Hours
Received	280.8	16.5	58.3	64.8	420.4
Retained	278.1	16.5	58.3	64.8	417.7

Appendix B: Empirical Sensitivity Estimation

To aid comparisons between data taken at different radar sensitivities, it is necessary to estimate the size to which a dataset is complete, *i.e.,* all objects of that size and larger are being detected. This quantity is strongly dependent on the range from the target due to the $1/R^4$ dependence of the radar range equation. To remove the range effects and focus on the noise-limiting characteristics of the receiver, a quantity is defined called "excess SNR" or XSNR. XSNR scales the measured RCS of all detections to a common range of 1000 km. In decibels, XSNR is defined as

$$XSNR_{dB} = RCS_{dB} - 40 \log_{10} \frac{R_{km}}{1000_{km}}$$

where RCS_{dB} is the measured RCS in decibels and R_{km} is the range of the detection in kilometers. The cumulative XSNR distribution typically follows a power law across a wide range of XSNR, from which a roll-off at smaller values can be easily and consistently determined from dataset to dataset. For the CY2020 HUSIR data, an automated process was developed to quantitatively and reproducibly determine the XSNR to which the data was 99%, 95%, and 90% complete. The process involves resampling of the cumulative XSNR distribution and finding the subset of resampled points that produce the best linear fit in log-log space. Ratios of the data to the fit are used to determine completeness levels. A full description of the process is presented in Appendix B of [3]. Here, the results of this process are presented for the CY2022, 75E dataset. There were not sufficient observation hours in the south staring datasets to make accurate estimates.

Figure B-1 shows, for the HUSIR CY2022, 75E dataset, the cumulative PP XSNR distribution with the original data as a blue line, the resampled points used in the fit as red "+" symbols, the linear fit as a dashed black line, and the XSNR levels for a data to model fit ratio of 99%, 95%, and 90% as red dashed, dotted, and dash-dotted vertical lines, respectively. When compared in this way, the 99% line corresponds roughly to where the data starts to diverge from the linear fit. It also turns out that the 95% completeness XSNR is comparable to the theoretical size of an object with a single-pulse SNR of 5.65 dB (the detection threshold set by MIT/LL, see Section 4.1) shown as a function of altitude in Section 4.2.3. In general, the completeness sizes estimated using this new method are consistent with previous estimates.

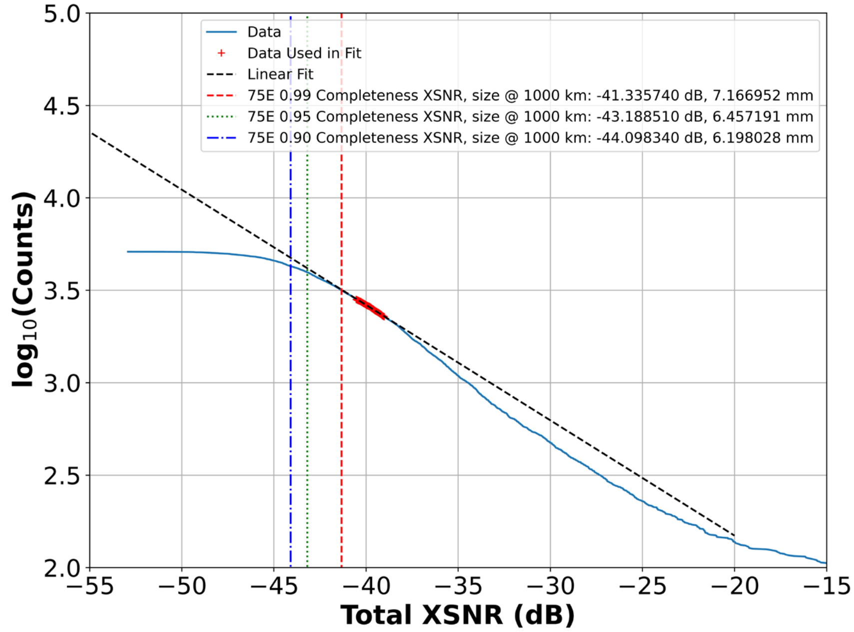

Figure B-1: HUSIR CY2022, 75E cumulative PP XSNR distribution with the original data as a blue line, the resampled points used in the fit as red "+" symbols, the fit as a dashed black line, and the XSNR levels of 99%, 95%, and 90% as red dashed, dotted, and dash-dotted vertical lines, respectively.

Appendix C: HUSIR 75° Elevation, East Pointing, 10.1 GHz

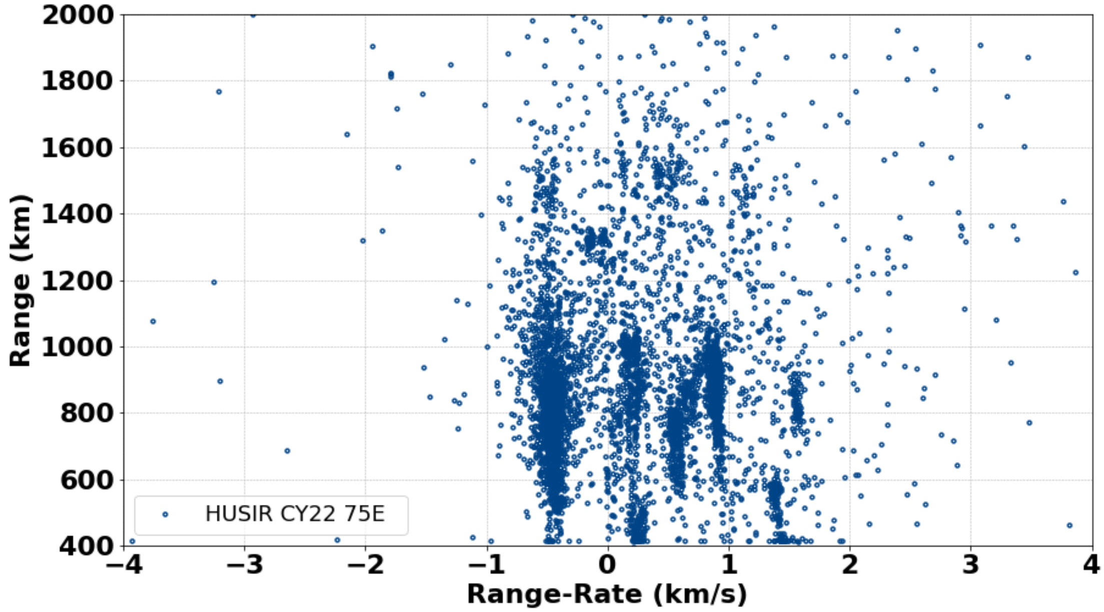

Figure C-1: Range versus Range-Rate, HUSIR 75E, CY2022.

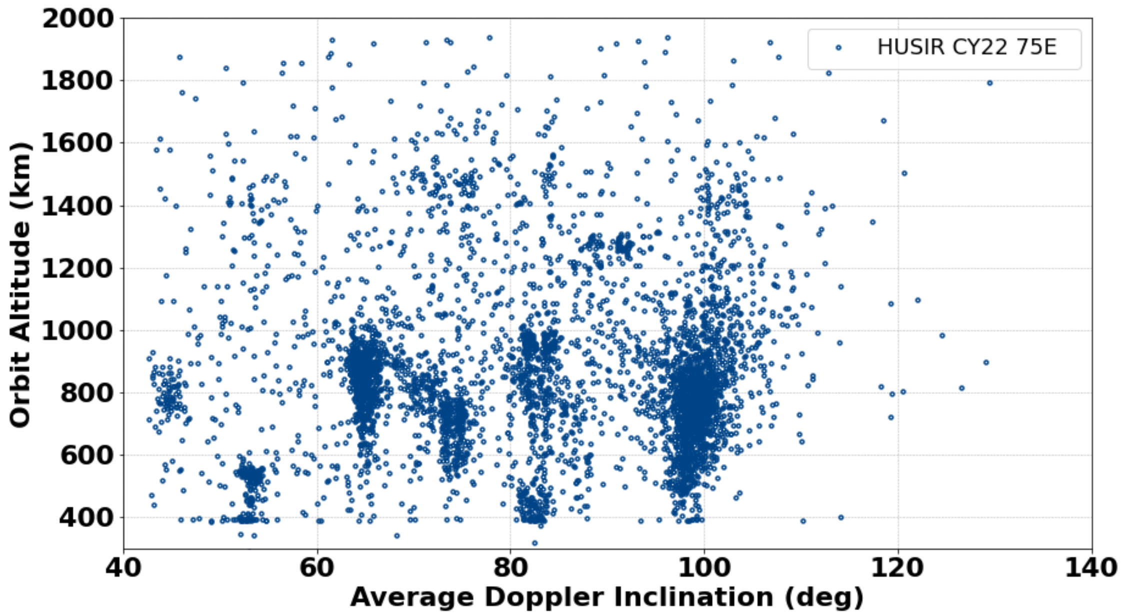

Figure C-2: Altitude versus Doppler inclination, HUSIR 75E, CY2022. Inclination derived from Range and Range Rate assuming a circular orbit.

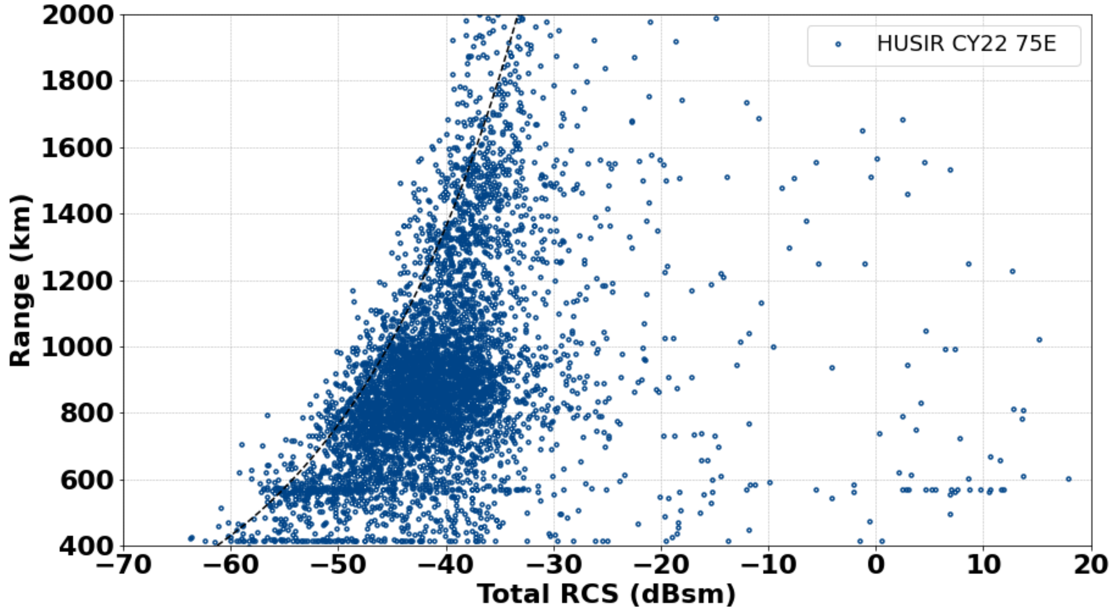

Figure C-3: Range versus Radar Cross Section, HUSIR 75E, CY2022. The black dashed line represents the range-dependent theoretical RCS of an object with a single-pulse SNR of 5.65 dB.

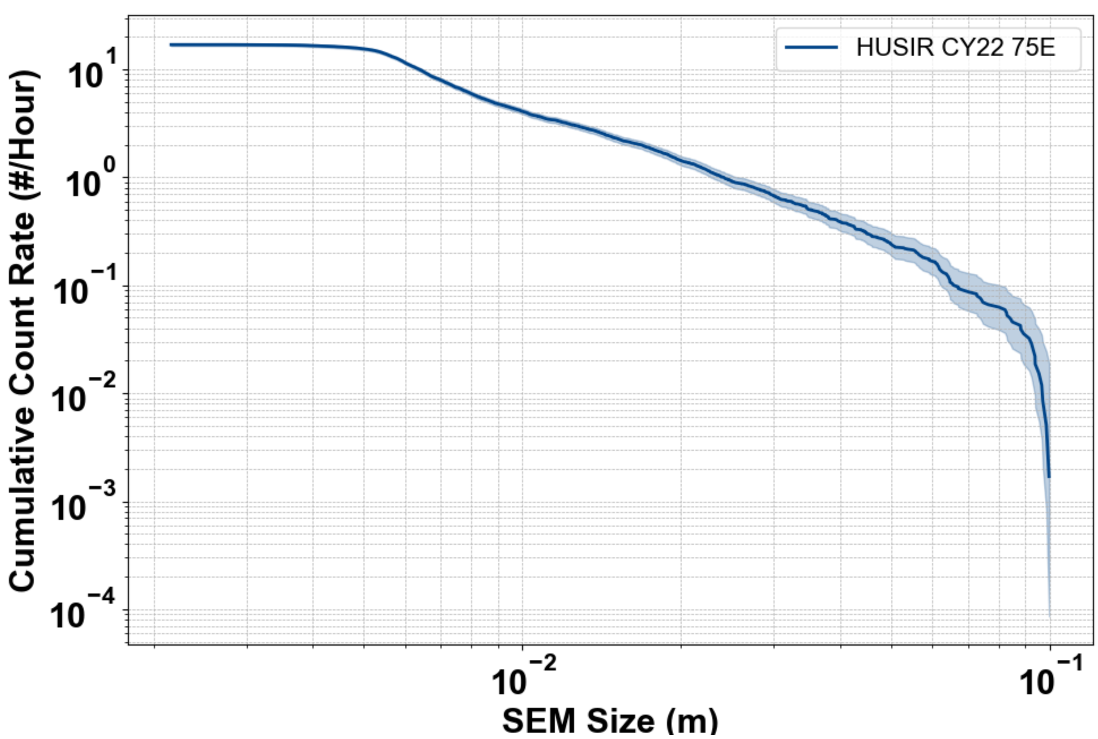

Figure C-4: Cumulative count rate versus SEM size limited to less than 10 cm, HUSIR 75E, CY2022. The shaded regions represent the 2σ uncertainty bounds.

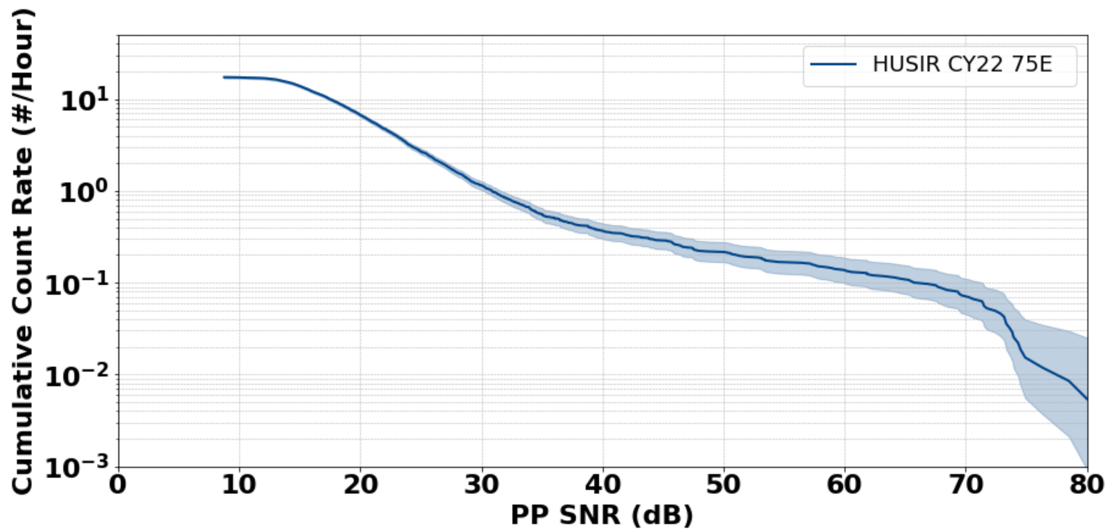

Figure C-5: Cumulative count rate versus detection SNR of the principal polarization, HUSIR 75E, CY2022. The shaded regions represent the 2σ uncertainty bounds.

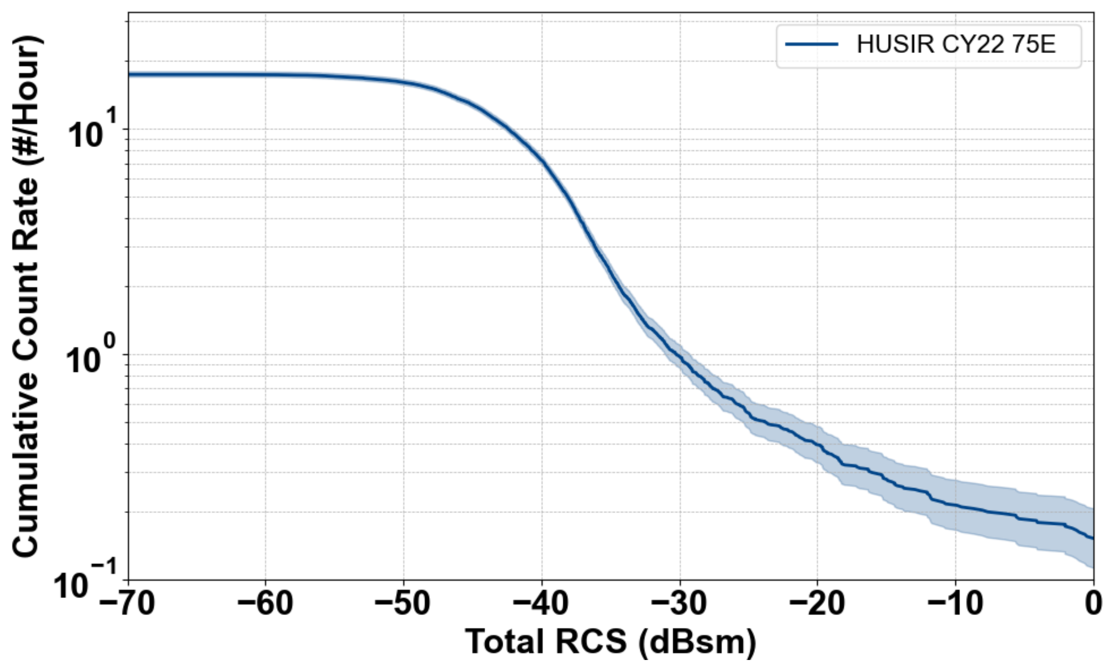

Figure C-6: Cumulative count rate versus Total Radar Cross Section, HUSIR 75E, CY2022. The shaded regions represent the 2σ uncertainty bounds.

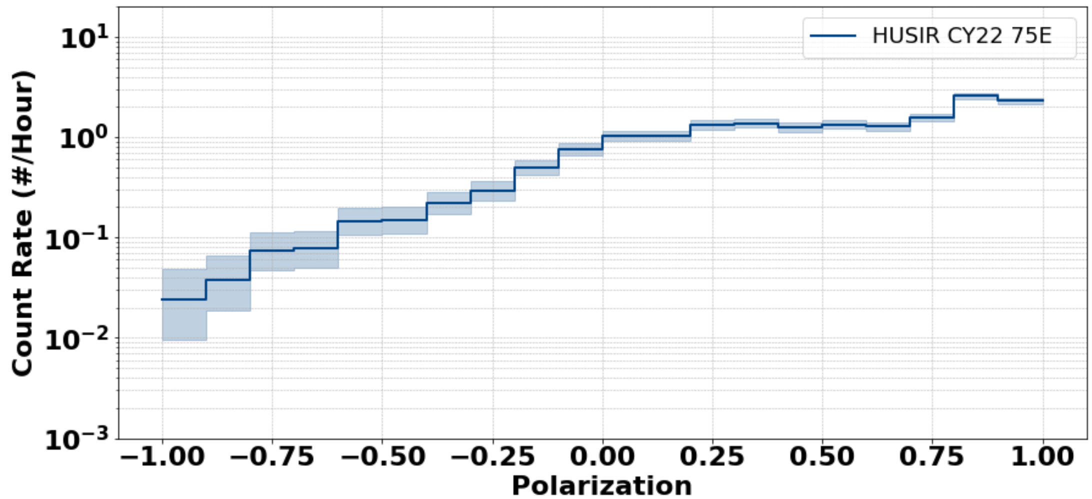

Figure C-7: Count Rate versus polarization ratio, HUSIR 75E, CY2022. The shaded regions represent the 2σ uncertainty bounds.

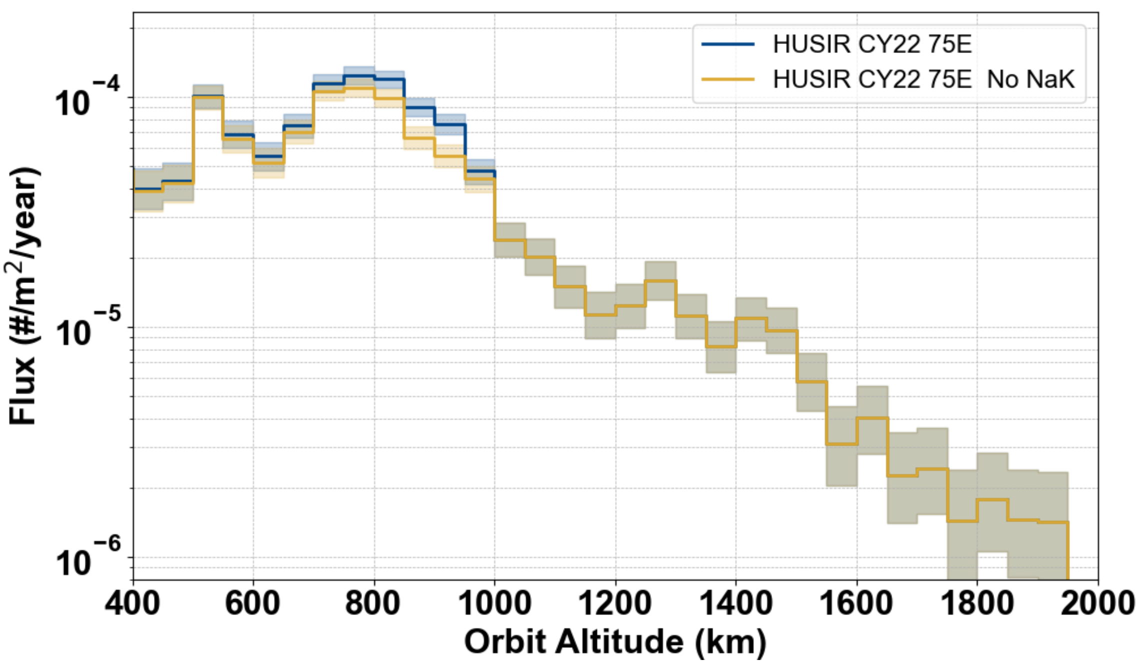

Figure C-8: Flux versus altitude, HUSIR 75E, CY2022 with and without NaK detections (No NaK). No size or altitude limits are applied. The shaded regions represent the 2σ uncertainty bounds.

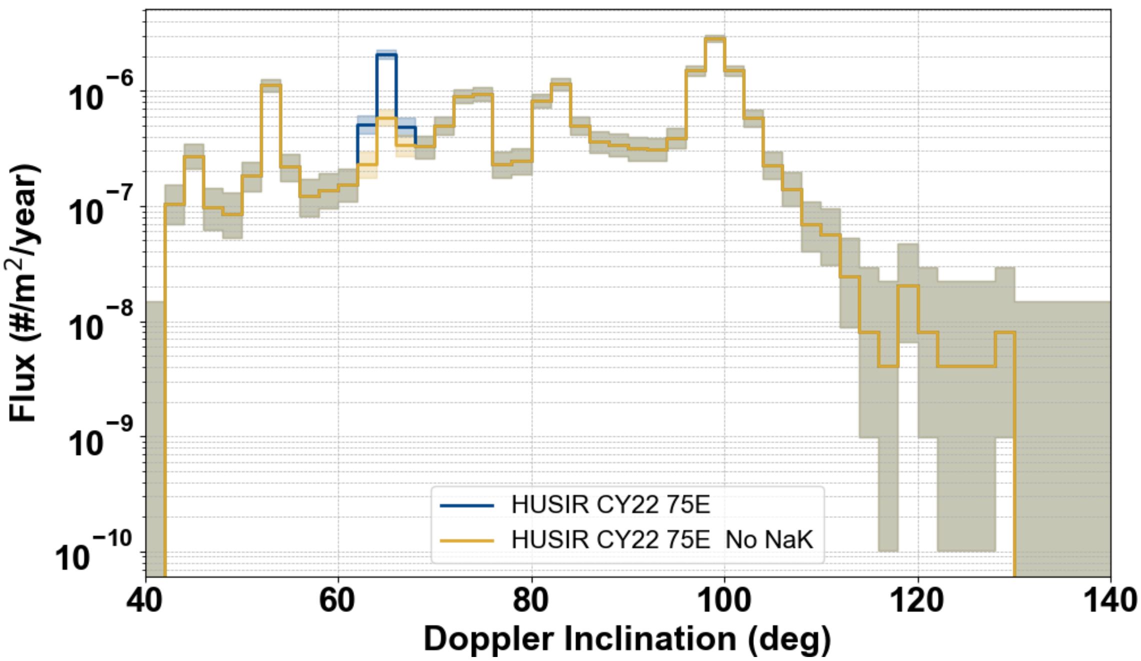

Figure C-9: Flux versus orbital inclination, HUSIR 75E, CY2022 with and without NaK detections (No NaK). No size or altitude limits are applied. The shaded regions

Appendix D: HUSIR 10° Elevation, South Pointing, 10.1 GHz

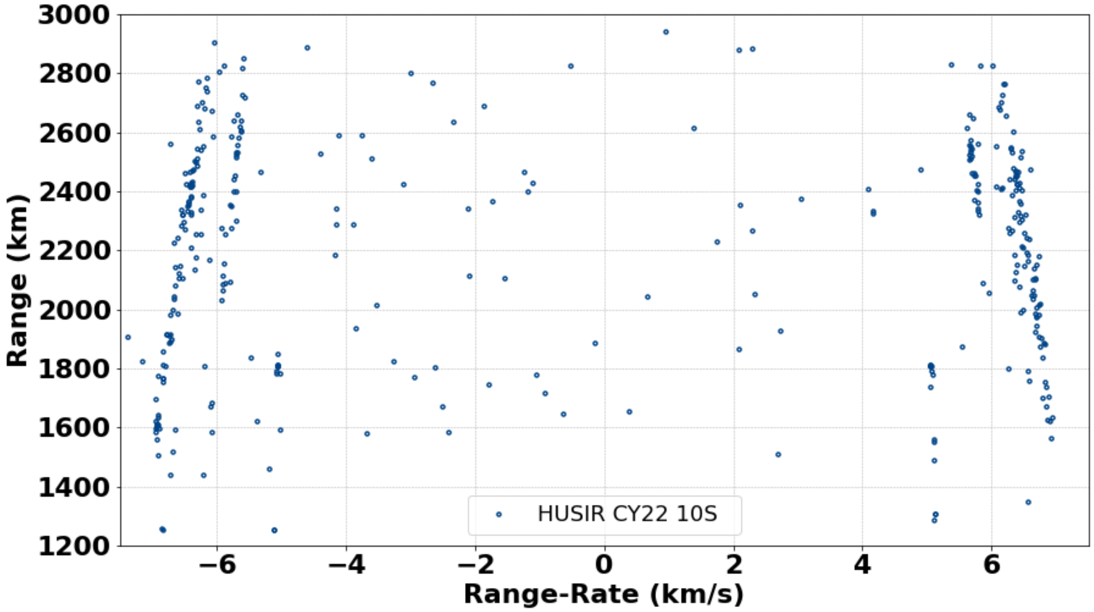

Figure D-1: Range versus Range-Rate, HUSIR 10S, CY2022.

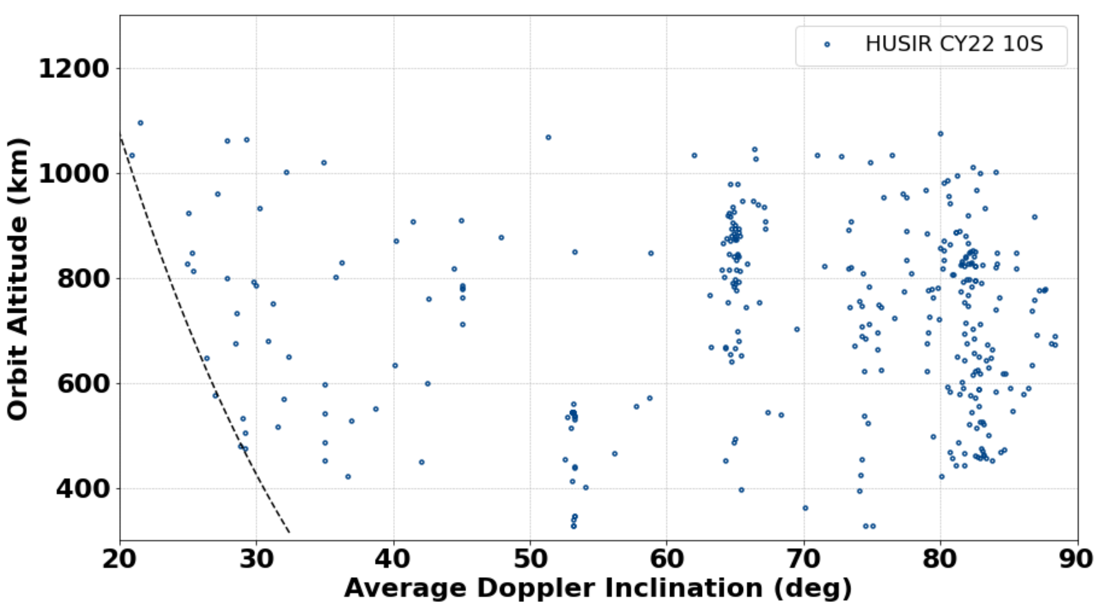

Figure D-2: Altitude versus Doppler inclination, HUSIR 10S, CY2022. Inclination derived from Range and Range-Rate assuming a circular orbit. The dashed black line represents the altitude-dependent minimum inclination visible to HUSIR.

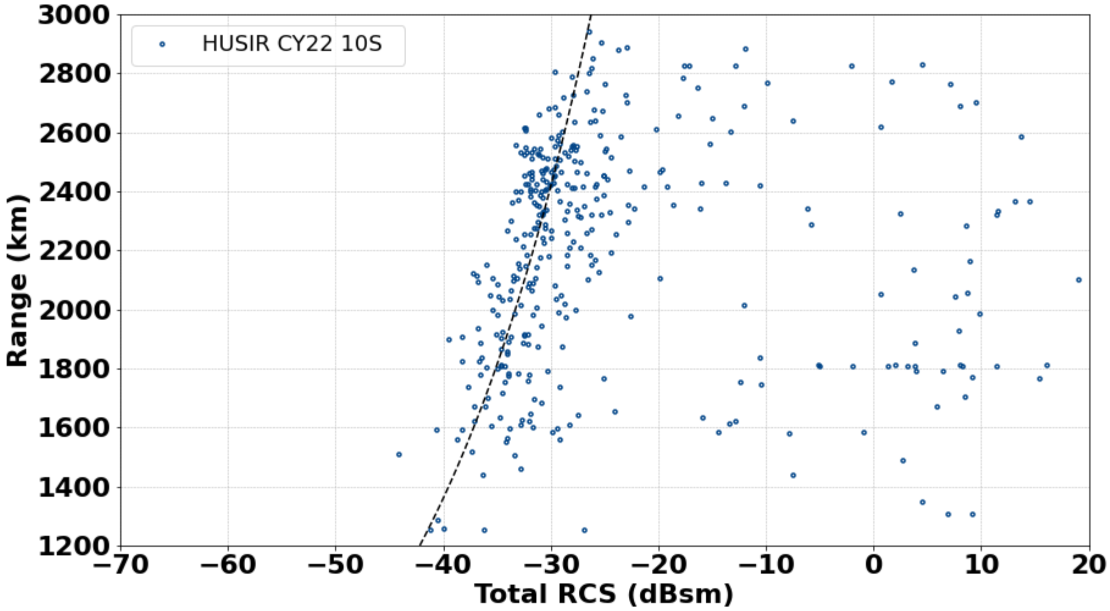

Figure D-3: Range versus Radar Cross Section, HUSIR 10S, CY2022. The black dashed line represents the range-dependent theoretical RCS of an object with a single-pulse SNR of 5.65 dB.

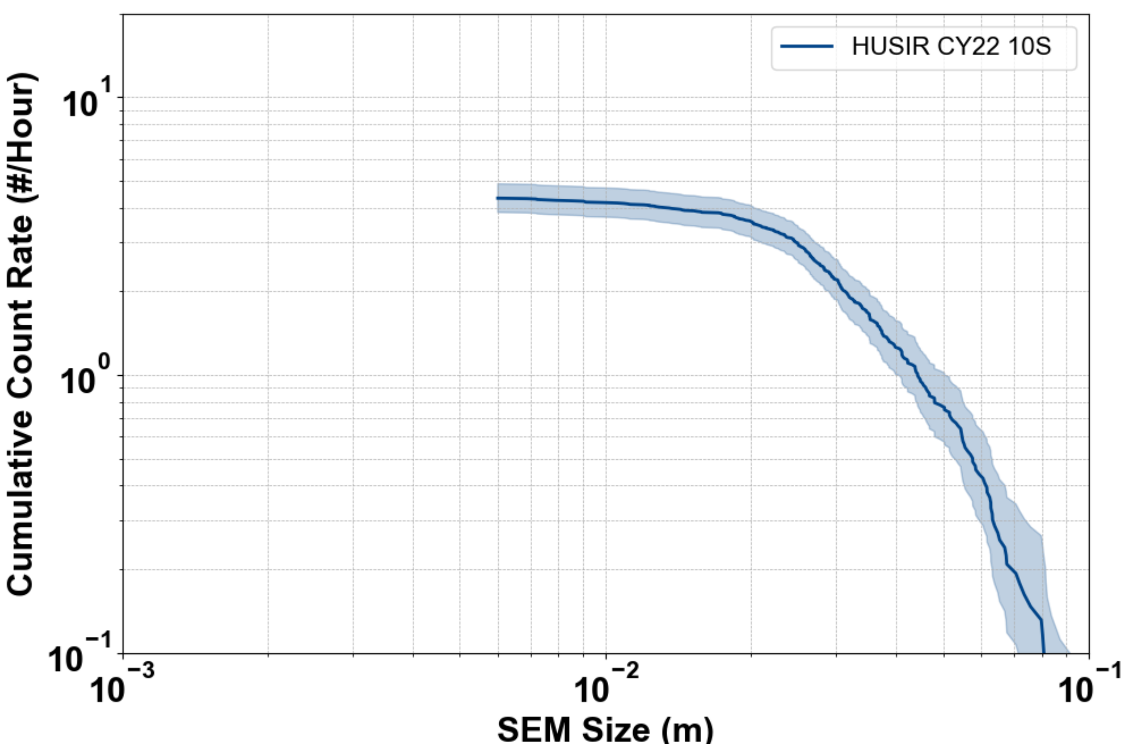

Figure D-4: Cumulative count rate versus SEM size, HUSIR 10S, CY2022. The shaded regions represent the 2σ uncertainty bounds.

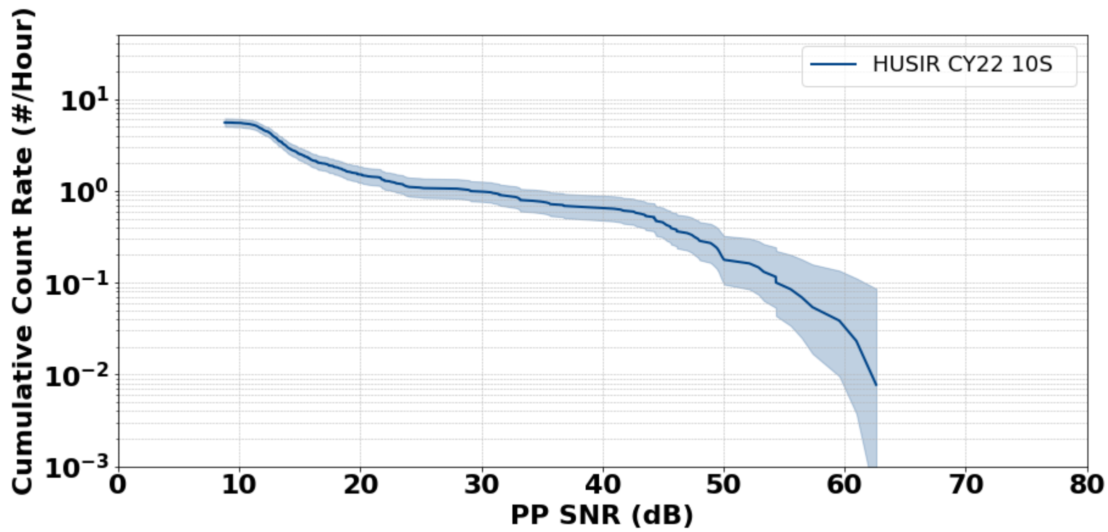

Figure D-5: Cumulative count rate versus detection SNR of the principal polarization, HUSIR 10S, CY2022. The shaded regions represent the 2σ uncertainty bounds.

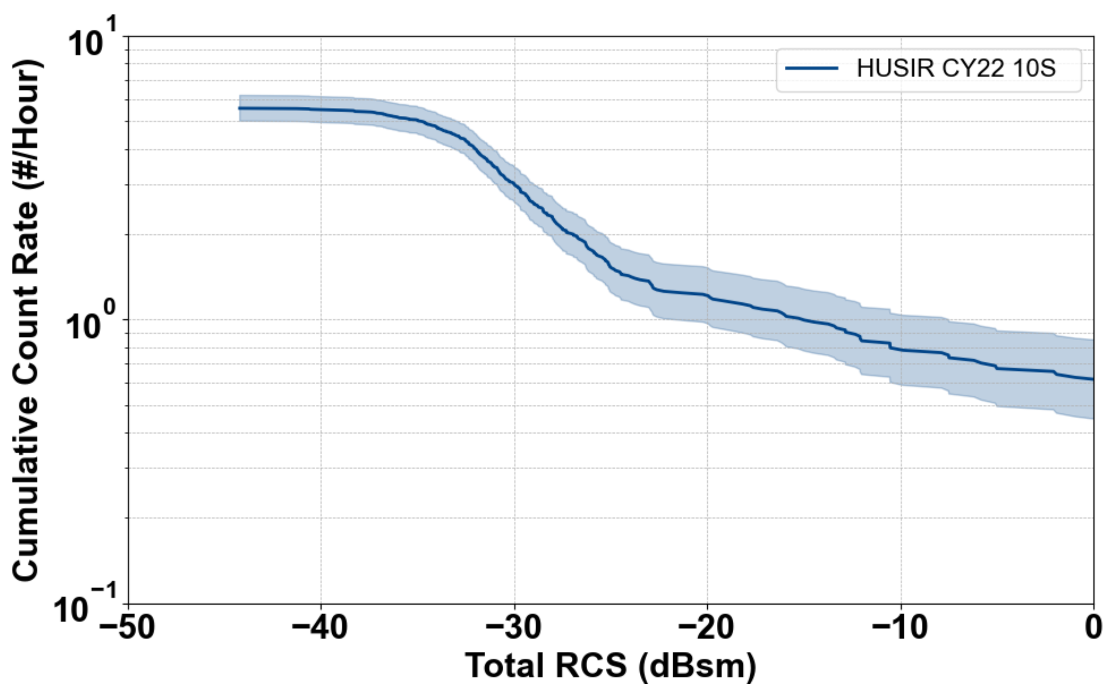

Figure D-6: Cumulative count rate versus Total Radar Cross Section, HUSIR 10S, CY2022. The shaded regions represent the 2σ uncertainty bounds.

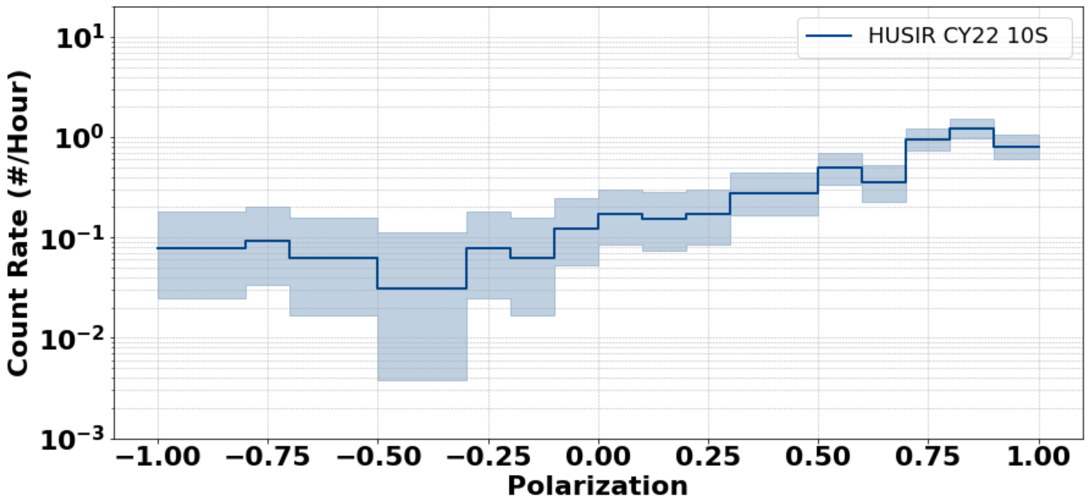

Figure D-7: Count Rate versus polarization ratio, HUSIR 10S, CY2022. The shaded regions represent the 2σ uncertainty bounds.

Appendix E: HUSIR 20° Elevation, South Pointing, 10.1 GHz

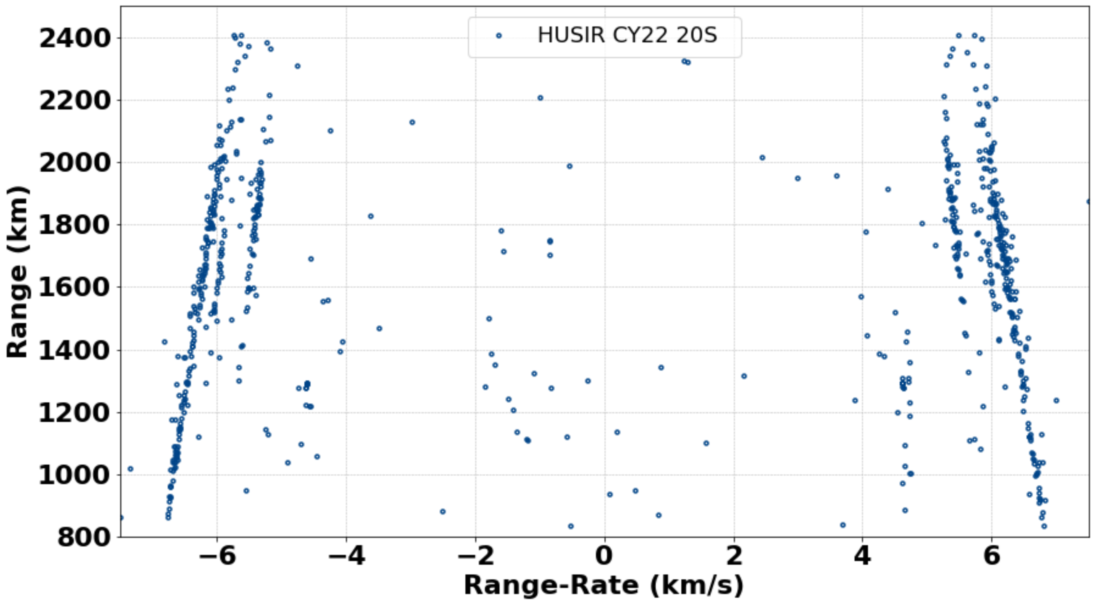

Figure E-1: Range versus Range-Rate, HUSIR 20S, CY2022.

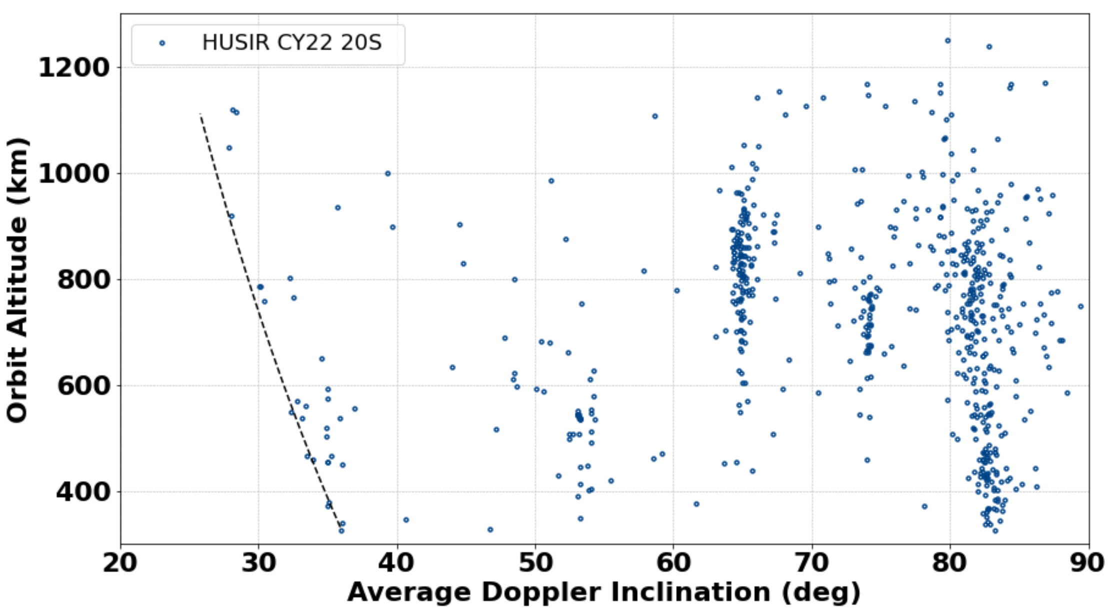

Figure E-2: Altitude versus Doppler inclination, HUSIR 20S, CY2022. Inclination derived from Range and Range-Rate assuming a circular orbit. The dashed black line represents the altitude-dependent minimum inclination visible to HUSIR.

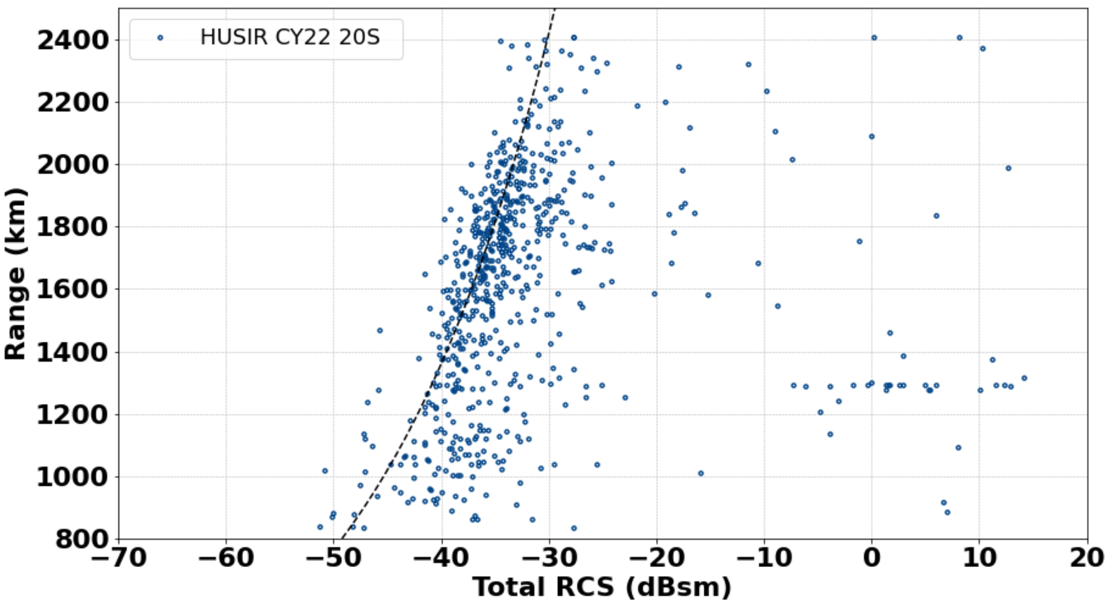

Figure E-3: Range versus Radar Cross Section, HUSIR 20S, CY2022. The black dashed line represents the range-dependent theoretical RCS of an object with an SNR of 5.65 dB. The line of objects from -10 to 10 Total RCS are likely members of the Starlink satellite constellation.

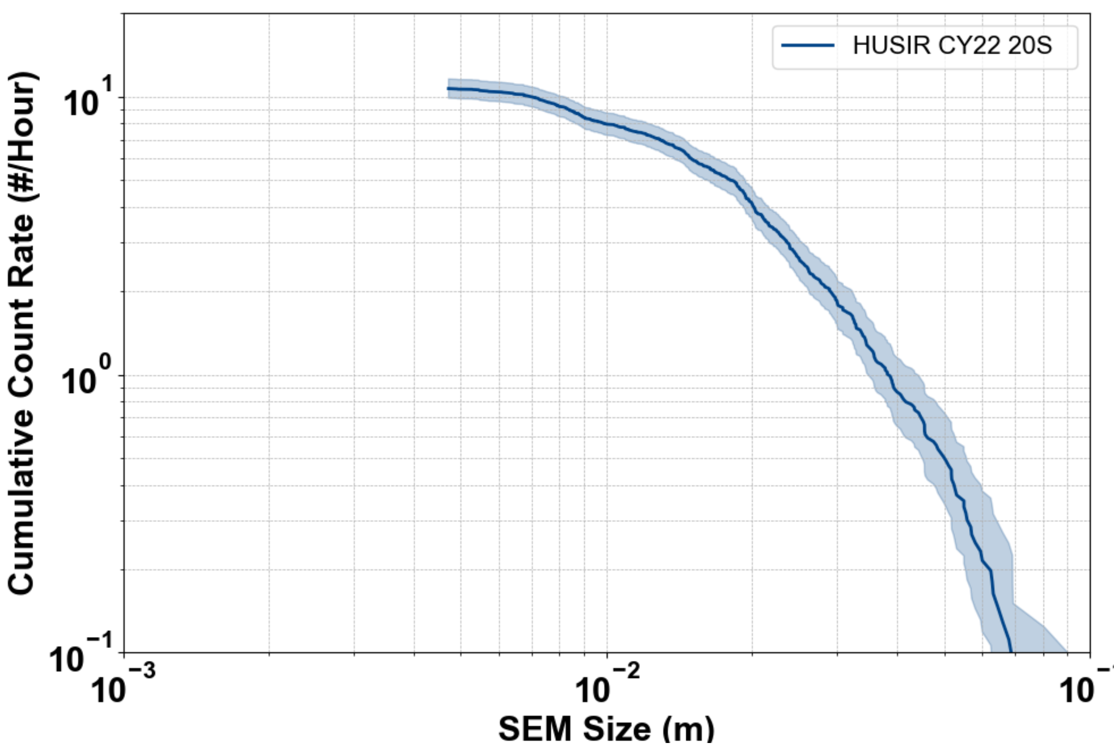

Figure E-4: Cumulative count rate versus SEM size, HUSIR 20S, CY2022. The shaded regions represent the 2σ uncertainty bounds.

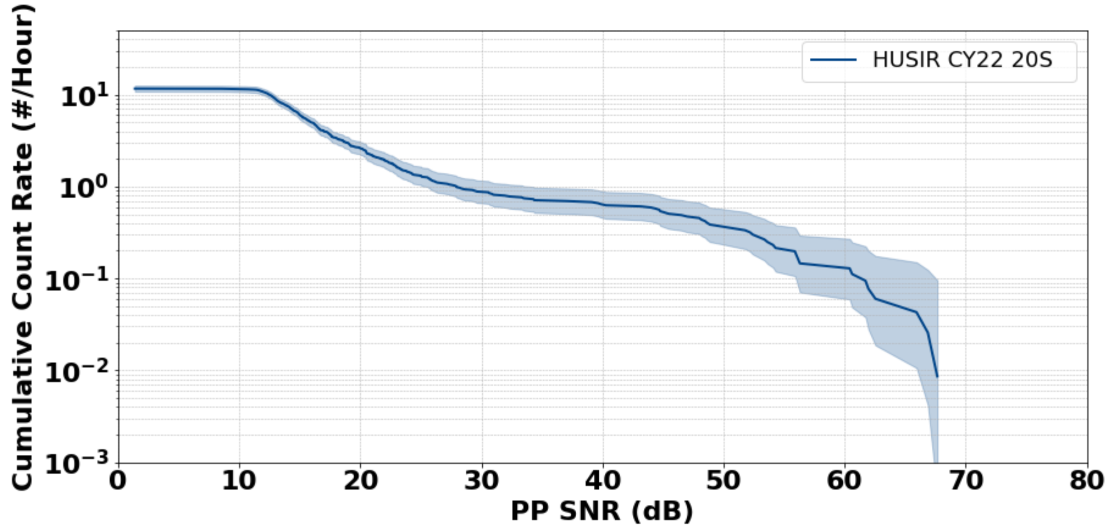

Figure E-5: Cumulative count rate versus detection SNR of the principal polarization, HUSIR 20S, CY2022. The shaded regions represent the 2σ uncertainty bounds.

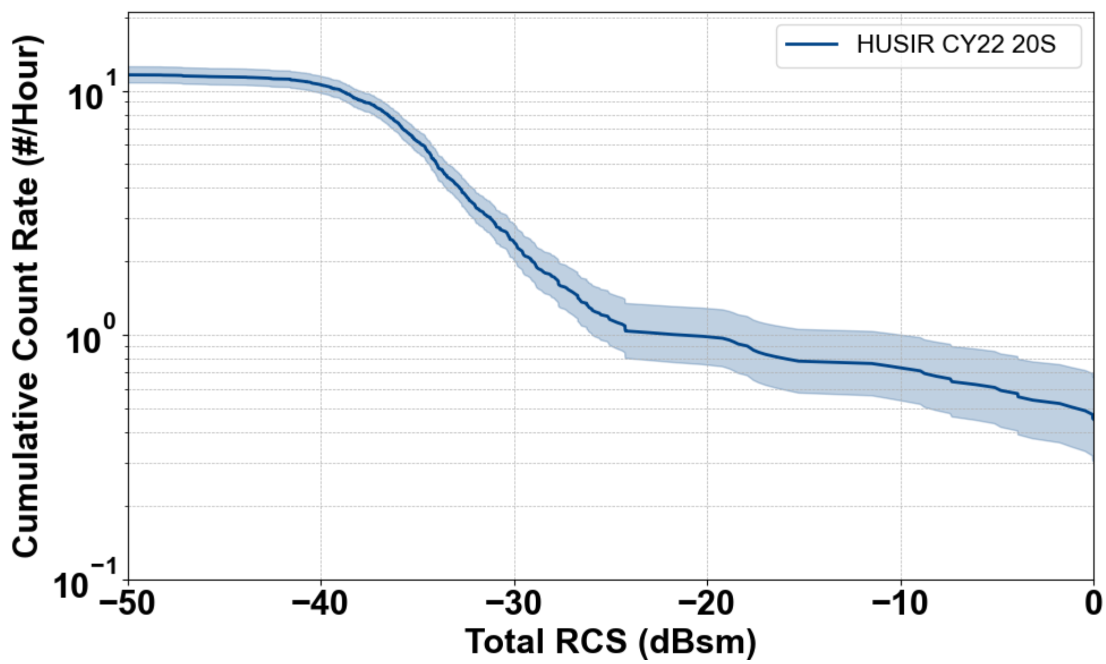

Figure E-6: Cumulative count rate versus Total Radar Cross Section, HUSIR 20S, CY2022. The shaded regions represent the 2σ uncertainty bounds.

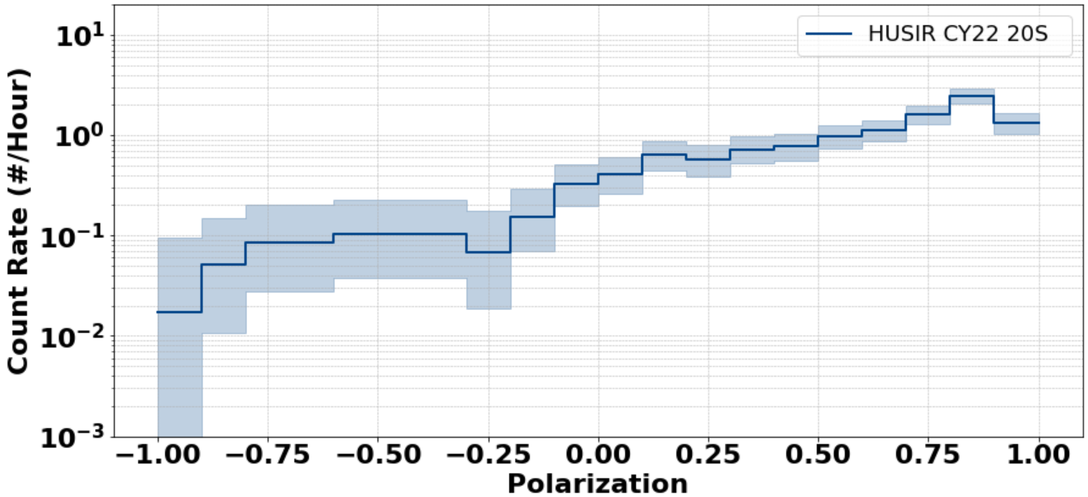

Figure E-7: Count Rate versus polarization ratio, HUSIR 20S, CY2022. The shaded regions represent the 2σ uncertainty bounds.